ARL TR-83-41

Copy No. 43

RAY MODELING METHODS FOR RANGE DEPENDENT OCEAN ENVIRONMENTS

Terry L. Foreman

APPLIED RESEARCH LABORATORIES
THE UNIVERSITY OF TEXAS AT AUSTIN
POST OFFICE BOX 8029, AUSTIN, TEXAS 78712-8029

1 December 1983

Technical Report

Prepared for:

NAVAL OCEAN RESEARCH
AND DEVELOPMENT ACTIVITY
NSTL STATION, MS 39529

UNCLASSIFIED

SECURITY CLASSIFICATION OF THIS PAGE (When Data Entered)

REPORT DOCUMENTATION PAGE		READ INSTRUCTIONS BEFORE COMPLETING FORM
1. REPORT NUMBER	2. GOVT ACCESSION NO. AD-A137 202	3. RECIPIENT'S CATALOG NUMBER
4. TITLE (and Subtitle) RAY MODELING METHODS FOR RANGE DEPENDENT OCEAN ENVIRONMENTS		5. TYPE OF REPORT & PERIOD COVERED technical report
		6. PERFORMING ORG. REPORT NUMBER ARL-TR-83-41
7. AUTHOR(s) Terry L. Foreman		8. CONTRACT OR GRANT NUMBER(s) N00014-82-C-0049
9. PERFORMING ORGANIZATION NAME AND ADDRESS Applied Research Laboratories The University of Texas at Austin Austin, Texas 78712-8029		10. PROGRAM ELEMENT, PROJECT, TASK AREA & WORK UNIT NUMBERS
11. CONTROLLING OFFICE NAME AND ADDRESS Naval Ocean Research and Development Activity NSTL Station, Mississippi 39529		12. REPORT DATE 1 December 1983
		13. NUMBER OF PAGES 91
14. MONITORING AGENCY NAME & ADDRESS (if different from Controlling Office)		15. SECURITY CLASS. (of this report) UNCLASSIFIED
		15a. DECLASSIFICATION/DOWNGRADING SCHEDULE

16. DISTRIBUTION STATEMENT (of this Report)

Approved for public release; distribution unlimited.

17. DISTRIBUTION STATEMENT (of the abstract entered in Block 20, if different from Report)

18. SUPPLEMENTARY NOTES

19. KEY WORDS (Continue on reverse side if necessary and identify by block number)

MEDUSA, ray, model, ocean, acoustic, eigenray, bathymetry, spline, caustic, ray trace, range dependent, propagation loss, transmission loss, bottom loss, bottom reflection, ray path, phase shift, ray theory, ray model, false caustic, multiple profile, cubic spline, numerical model, numerical ray trace, sound speed profile, sound velocity profile

20. ABSTRACT (Continue on reverse side if necessary and identify by block number)

This report describes mathematical, numerical, and software design methods for ray models for range dependent ocean environments. Numerical techniques are described for solving ray path and intensity differential equations and for computing path length and travel time integrals. Modified cubic splines fit the bathymetry and sound speed profiles with the degree of mathematical smoothness required to eliminate false caustics and shadow zones, while avoiding non-physical excursions sometimes observed in standard splines. Several new interpolation procedures yield eigenray path information.

DD FORM 1 JAN 73 1473 EDITION OF 1 NOV 65 IS OBSOLETE

UNCLASSIFIED

SECURITY CLASSIFICATION OF THIS PAGE (When Data Entered)

TABLE OF CONTENTS

LIST OF FIGURES

I. INTRODUCTION

It is frequently important for the analysis of propagation of sound in the ocean to be able to compute the acoustic field in a range dependent ocean environment. Although good computational methods have been developed for modeling acoustic propagation in horizontally stratified acoustic media, range variations in the environment play such an important role in many realistic propagation problems that the simplifying assumption of horizontal stratification is not justified.

The methods available for modeling sound propagation in a range variable medium may be roughly categorized as wave theoretical and ray theoretical. Reference 1 is a survey of these methods.

Wave theoretical methods applicable to range dependent environments include the adiabatic normal mode approach,[2] horizontal ray theory,[3,4] the parabolic equation method,[5] coupled mode theory,[6,7] and direct numerical solution of the wave equation. All but the last of these procedures make use of various approximations in order to reduce the required computational effort. The approximations are valid only for gradual variations of the media with range. The direct numerical approach is computationally very intensive and may not be practical to implement except on the largest and fastest scientific computers. For all of these models, the amount of computation required increases rapidly with increasing acoustic wave number, so the models are effectively limited to low frequency applications. The principal advantages of wave models are the correct treatment of diffraction effects and the ability to correctly model complex bottom interaction effects.

The principal advantage of ray theory, on the other hand, is that the paths of energy propagation through the medium are explicitly

identified. The ability to single out the energetically important propagation paths appeals to physical intuition and is very useful for gaining an understanding of the important influences on propagation.

The convenience of the ray theory formulation is achieved at the cost of an approximation. The ray theory approximation and the approximations made in practical wave models, together with the computational limitations on wave models, are such that the advantages and limitations of ray models and wave models are almost the reverse of each other. Wave models are limited to low frequencies; ray models are most accurate at high frequencies. Wave models include diffraction and boundary interaction effects; uncorrected ray models neglect diffraction effects and have less sophisticated treatments of boundaries. Wave models are inaccurate to varying degrees near sources, particularly in the extreme nearfield; ray models grow more accurate as one approaches the source. Most wave models can tolerate almost any variation of the environment with depth, but ray models can better tolerate range variations.

In recent years, ray models have benefited from the development of correction formulas which introduce diffraction effects[8,9] and improve the treatment of boundaries.[10]

The author's involvement with ray models began in 1976 with his development and implementation of a range independent ray model[11] at Applied Research Laboratories, The University of Texas at Austin (ARL:UT). Prior to that time, several range dependent ray models had already been implemented at other facilities.[12,13] All of these, however, suffered from various deficiencies, including the representation of the acoustic media, methods for tracing rays (determining the paths of energy propagation), the location of eigenrays (finding the rays which travel from the source to an observation point or receiver), the calculation of acoustic pressure along a ray path, and the design and implementation of the software itself. These problems are not at all independent of each other and the adverse consequences of an inadequate solution to any one

of them will usually be compounded in several others. Nor could these difficulties reasonably be anticipated; all were uncovered by attempting to build and use practical models.

In 1980, with U.S. Navy funding, the author undertook to develop a new range dependent ray model. The effort drew on several years of experience in numerical modeling and borrowed heavily from existing ray models and published research. The result is the ray model MEDUSA, which, after three years of development, testing, and revision, is being released to a growing number of research and prediction facilities.

The methods developed to redress the problems inherent in ray modeling are the subject of this report. The techniques are developed and explained. Considerable attention is also given to the pitfalls of ray modeling and to seemingly plausible procedures, often used, which do not work. Always, the focus is on the means of implementing practical, reliable ray models on scientific computers.

The remainder of this report is organized as follows. The ray path and intensity equations are derived in Chapter II. The procedures for solving these equations are described in Chapter III. The methods for computing the sound speed, sound speed gradients with respect to depth and range, and the bathymetry (the ocean bottom depth as a function of range from the source), given only tabulated samples of these quantities, are described in Chapter IV. Chapter V covers the methods used to determine the eigenray launch angles and to compute eigenray path data, such as travel times and arrival angles. Chapter VI is an overview of the organization of the MEDUSA model. The report concludes in Chapter VII with a typical application of MEDUSA.

II. REVIEW OF RAY THEORY

Brief derivations of the ray path and intensity equations are presented here to establish the notation and coordinate system conventions and to provide background for the development of the specialized equations used in MEDUSA. More extensive treatments of ray theory are available in several texts.[14-16]

The acoustic wave equation for pressure $P(\vec{r},t)$,

$$\nabla^2 P = \frac{1}{c^2(\vec{r})} \frac{\partial^2 P}{\partial t^2} \quad , \tag{II.1}$$

becomes, upon assuming $P(\vec{r},t)=A(\vec{r})e^{j\phi(\vec{r})-j\omega t}$,

$$A\left[k^2 - \vec{\nabla}\phi\cdot\vec{\nabla}\phi + \frac{\nabla^2 A}{A}\right] + j\left[2\vec{\nabla}A\cdot\vec{\nabla}\phi + A\nabla^2\phi\right] = 0 \quad , \tag{II.2}$$

where $k=\omega/c$ is the wave number and ϕ represents an expanding wave front. Since A and ϕ are assumed to be real functions, the terms in brackets in Eq. II.2 must vanish separately and identically:

$$\left|\vec{\nabla}\phi\right|^2 = K^2 \quad , \tag{II.3}$$

$$2\vec{\nabla}A\cdot\vec{\nabla}\phi + A\nabla^2\phi = 0 \quad , \tag{II.4}$$

where $K^2 = k^2 + \nabla^2 A/A$.

Surfaces of constant phase, ϕ, are wave fronts. The outward normals to these surfaces, parallel to the vector $\vec{\nabla}\phi$, indicate the directions of wave propagation. Equation II.3, the eikonal equation, gives rise to equations for ray paths which are perpendicular to the wave fronts. Equation II.4, the transport equation, leads to equations for intensity along the ray paths.

The intensity at a point on a ray path is[16]

$$I = \frac{PP^*}{2\rho c} = \frac{A^2}{2\rho c} \quad , \tag{II.5}$$

where ρ is the density of the medium. For two points located on a ray and both points in the water, ρ and c are constant to within a few percent, so the intensity ratio at the two points is given approximately by

$$\frac{I_2}{I_1} = \frac{A_2^2}{A_1^2} \quad , \tag{II.6}$$

where the subscripts indicate the two points. We now seek an expression for A_2^2/A_1^2.

The volume V, shown in Fig. 1, is enclosed by the surface S, defined by the wavefront surface sections W_1 and W_2 and the four ray paths resulting from a small change $\delta\theta_s$ in the ray source depression

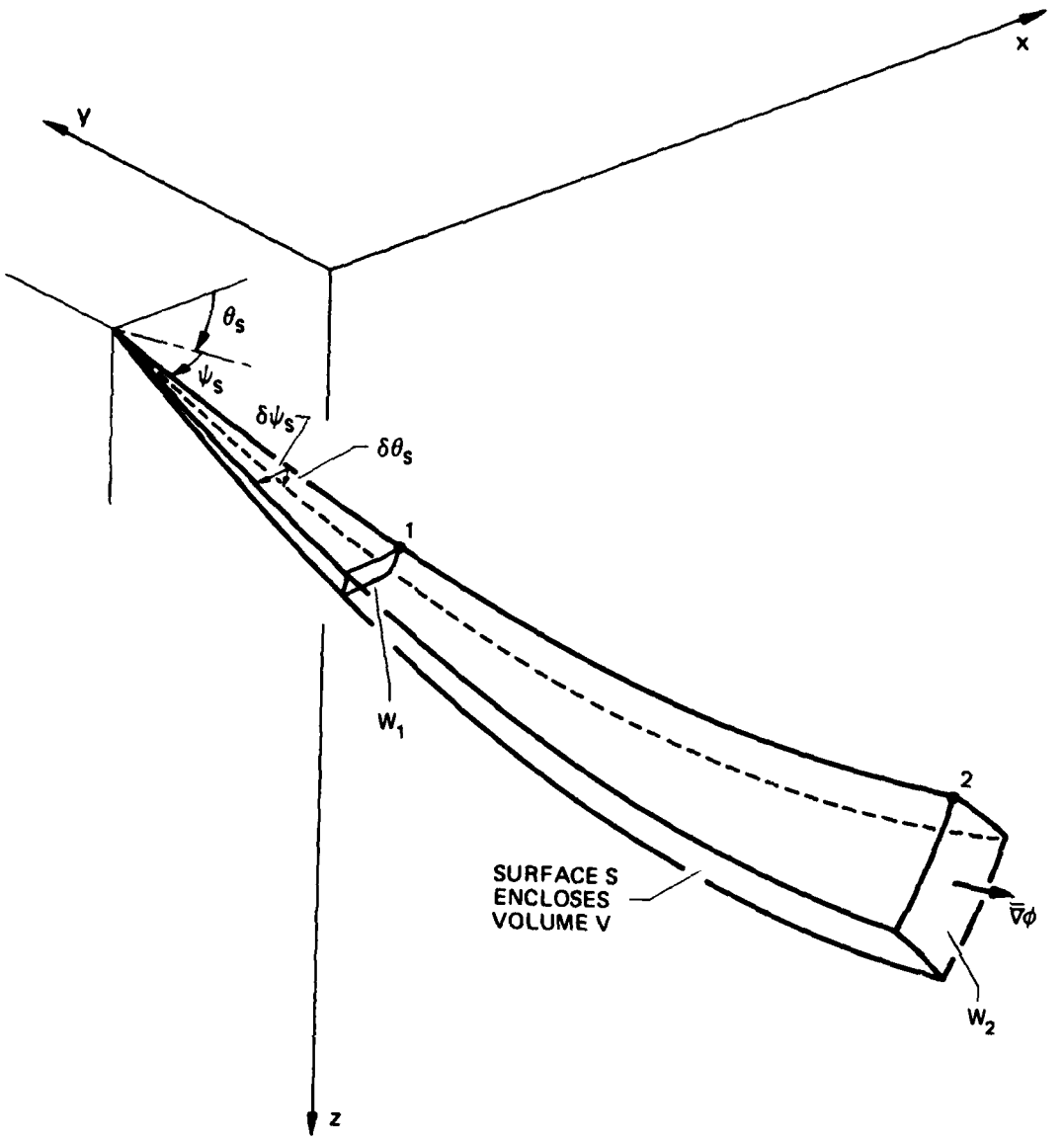

FIGURE 1
RAY PATH SPREADING IN AN INHOMOGENEOUS MEDIUM

ARL-UT
AS-82-1665
TLF-GA
10-19-82

angle θ_s, and a small change $\delta\psi_s$ in the azimuthal source angle ψ_s. Noting that Eq. II.4 can be written as a divergence,

$$\vec{\nabla}\cdot(A^2\vec{\nabla}\phi) = 0 \quad , \tag{II.7}$$

one obtains by Gauss' theorem

$$\int_V dV\vec{\nabla}\cdot(A^2\vec{\nabla}\phi) = \int_S dS\hat{n}\cdot A^2\vec{\nabla}\phi \quad , \tag{II.8}$$

where $\hat{n}$ is the outward unit vector normal to S. Since $n\cdot\vec{\nabla}\phi=0$ along the ray paths by definition, the only contributions to the integral occur at the end surfaces W_1 and W_2. Since $\vec{\nabla}\phi$ is always directed away from the source one has, from Eq. II.3,

$$\hat{n} = \begin{cases} (\vec{\nabla}\phi)/K \text{ on } W_1 \\ -(\vec{\nabla}\phi)/K \text{ on } W_2 \end{cases} . \tag{II.9}$$

Hence,

$$\int_{W_2} A^2 K dW = \int_{W_1} A^2 K dW \quad . \tag{II.10}$$

For infinitesimal variations in launch angles, the integrands will be constants on the surfaces W_1 and W_2, so from Eq. II.10,

$$\frac{A_2^2 K_2}{A_1^2 K_1} = \frac{\int_{W_1} dW}{\int_{W_2} dW} \quad . \tag{II.11}$$

Thus far the only approximation made has been the assumption that ρ and c are nearly constant in the water.

If A varies slowly over a wavelength, which will ordinarily be true for high frequencies, slow spatial variations in c, and in the absence of nearby boundaries, then

$$k^2 >> \frac{\nabla^2 A}{A} \quad . \tag{II.12}$$

Inequality II.12 is the ray theory approximation. When it is valid, $K \simeq k$ and, since $k_1 \simeq k_2$ in the water,

$$\frac{I_2}{I_1} = \frac{A_2^2}{A_1^2} = \frac{\int_{W_1} dW}{\int_{W_2} dW} \quad . \tag{II.13}$$

Equation II.13 states that the intensity ratio is inversely proportional to the ratio of the infinitesimal areas of W_1 and W_2.

We now seek differential equations for the ray paths. Recall that $\vec{\nabla}\phi$ defines the direction of ray propagation. The unit vector in the direction of the ray path is, by Eq. II.3, $\vec{\nabla}\phi/K$. If s is ray path length and $\vec{x}(s)$ is the ray path position vector, then $d\vec{x}/ds$ is also the unit vector in the direction of the ray path, so

$$K \frac{d\vec{x}}{ds} = \vec{\nabla}\phi \quad . \tag{II.14}$$

Differentiation of Eq. II.14 with respect to path length yields

$$\frac{d}{ds}\left(K \frac{d\vec{x}}{ds}\right) = \frac{d}{ds} \vec{\nabla}\phi \quad . \tag{II.15}$$

But, using the vector operator identity $d/ds = d\vec{x}/ds \cdot \vec{\nabla}$ and the fact that $\vec{\nabla}\phi = K d\vec{x}/ds$, the right hand side of Eq. II.15 can be simplified:

$$\begin{aligned}
\frac{d}{ds} \vec{\nabla}\phi &= \left(\frac{d\vec{x}}{ds} \cdot \vec{\nabla}\right)\left(\hat{x} \frac{\partial\phi}{\partial x} + \hat{y} \frac{\partial\phi}{\partial y} + \hat{z} \frac{\partial\phi}{\partial z}\right) \\
&= \hat{x} \frac{\vec{\nabla}\phi}{K} \cdot \frac{\partial}{\partial x}\vec{\nabla}\phi + \hat{y} \frac{\vec{\nabla}\phi}{K} \cdot \frac{\partial}{\partial y}\vec{\nabla}\phi + \hat{z} \frac{\vec{\nabla}\phi}{K} \cdot \frac{\partial}{\partial z}\vec{\nabla}\phi \\
&= \frac{1}{2} \frac{1}{K}\left(\hat{x} \frac{\partial}{\partial x} + \hat{y} \frac{\partial}{\partial y} + \hat{z} \frac{\partial}{\partial z}\right)(\vec{\nabla}\phi \cdot \vec{\nabla}\phi) \\
&= \frac{1}{2} \frac{1}{K} \vec{\nabla} K^2 \\
&= \vec{\nabla} K \quad .
\end{aligned} \tag{II.16}$$

If we again invoke the ray theory approximation (replacing K by k), then Eq. II.16 becomes

$$\frac{d}{ds}\left(k\,\frac{d\vec{x}}{ds}\right) = \vec{\nabla}k \quad . \tag{II.17}$$

The replacement of K by k enables one to factor out ω from Eq. II.17, making explicit the frequency independence of ray theory. Division of Eq. II.17 by ω/c_0 yields

$$\frac{d}{ds}\left(n\,\frac{d\vec{x}}{ds}\right) = \vec{\nabla}n \quad , \tag{II.18}$$

where c_0 is an arbitrary reference sound speed and $n=c_0/c$ is the index of refraction. Equation II.18 is the ray path equation.

The two basic functions of a ray model are to solve the ray path equation and then to compute intensities at desired points on the ray paths by determining the ratio of the areas of W_1 and W_2. In the next two sections differential equations are derived for the ray paths and intensities in forms suitable for solution on a digital computer.

A. Ray Path Equations in an Azimuthally Symmetrical Environment

The source is now assumed to lie on the vertical axis of a cylindrical coordinate system (see Fig. 2) and the sound speed and bathymetry are assumed to be azimuthally symmetrical about the vertical axis.

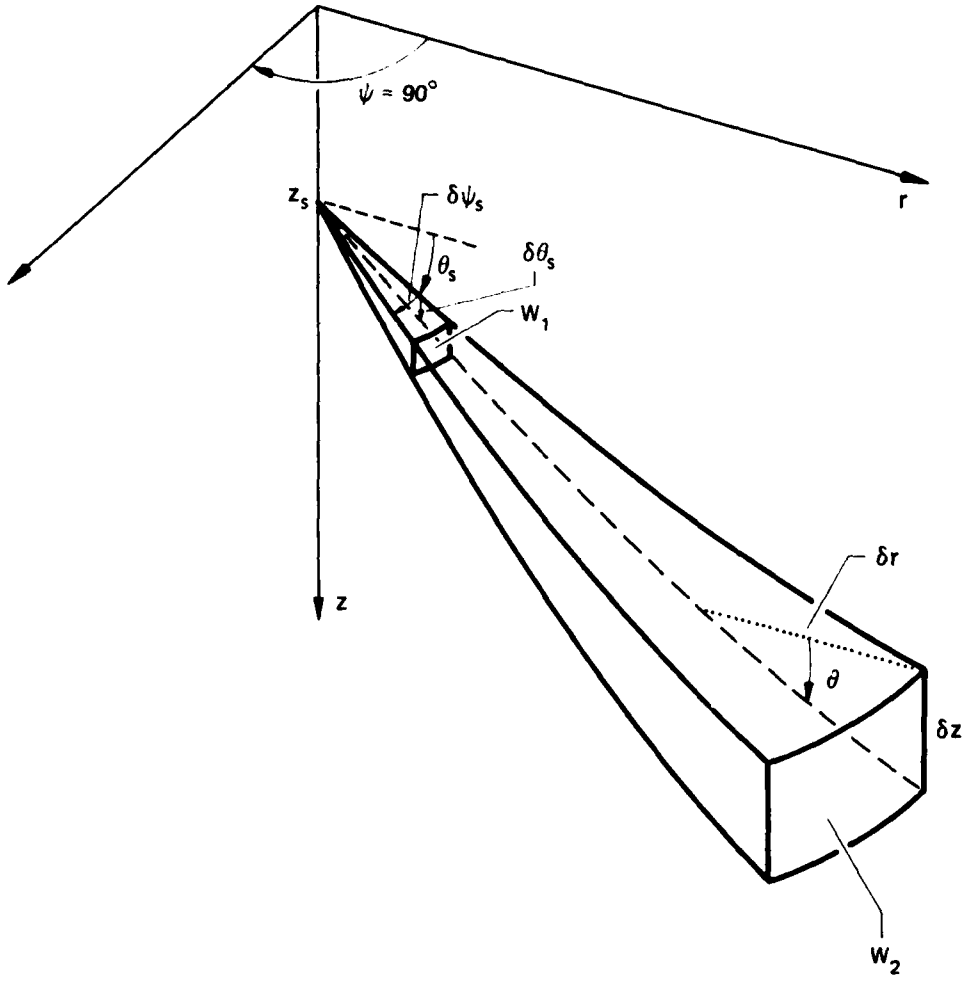

FIGURE 2
RAY PATH SPREADING IN AN AZIMUTHALLY SYMMETRICAL MEDIUM

ARL:UT
AS-82-1666
TLF - GA
10-19-82

If we equate vector components on the left- and right-hand sides of the ray path equation (Eq. II.18), we obtain equations for the ray path position coordinates in terms of the path length. In the cylindrical coordinate system depicted in Fig. 2, the ray path coordinates are range (r), depth (z), and azimuthal angle (ψ). In scalar form, Eq. II.18 becomes

$$\frac{d}{ds}\left(n\,\frac{dz}{ds}\right) = \frac{\partial n}{\partial z} \quad , \tag{II.19a}$$

$$\frac{d}{ds}\left(n\,\frac{dr}{ds}\right) - rn\left(\frac{d\psi}{ds}\right)^2 = \frac{\partial n}{\partial r} \quad , \tag{II.19b}$$

and

$$\frac{d}{ds}\left(r^2 n\,\frac{d\psi}{ds}\right) = \frac{\partial n}{\partial \psi} \quad . \tag{II.20c}$$

If, for convenience, the ray azimuthal angle at the source, ψ_s, is taken to be zero, then the solution to Eq. II.19c is simply $\psi(s)=0$, because the azimuthal symmetry of the environment assures that rays which originate in the r-z plane remain in the r-z plane. We therefore need only concern ourselves with Eqs. II.19a and II.19b.

Equations II.19a and II.19b are parametric second order nonlinear equations for the ray path position coordinates r and z in terms of the path length s. These two equations can be combined in a single second order nonlinear differential equation for path depth z as a function of range r by changing the independent path parameter from path length to range. The change of variable is accomplished using the

relation $d/ds = \cos\theta\, d/dr$, where θ is the vertical ray path angle, or depression angle (see Fig. 2). With the change of independent variable, and using $d\psi/ds=0$, Eqs. II.19a and II.19b become

$$\frac{dz}{dr}\cos\theta\,\frac{d}{dr}(n\cos\theta) + n\cos^2\theta\,\frac{d^2z}{dr^2} = n_z \qquad \text{(II.20a)}$$

and

$$\cos\theta\,\frac{d}{dr}(n\cos\theta) = n_r \quad , \qquad \text{(II.20b)}$$

where n_z and n_r are the depth and range gradients of n. Substitution of Eq. II.20b into Eq. II.20a then gives

$$z'' = (1+z'^2)\left(\frac{n_z}{n} - z'\,\frac{n_r}{n}\right) \quad , \qquad \text{(II.21)}$$

where primes denote differentiation with respect to r.

The initial values required for solution of the path equations are obtained from the source position and ray launch angle:

$$z(0) = z_s \qquad \text{(II.22)}$$

and

$$z'(0) = \tan\theta_s \quad , \qquad \text{(II.23)}$$

where z_s is the source depth and θ_s is the launch depression angle (see Fig. 2).

Whenever a ray undergoes a surface or bottom reflection, the solution of the path equation must be restarted at the boundary intersection with a new ray path slope. The ray path slope upon specular reflection, z'_R, is calculated from the incident ray path slope, z'_I, and the ocean bottom slope, z'_B, if applicable. In the case of a surface reflection, the reflected ray path slope is

$$z'_R = -z'_I \quad . \tag{II.24}$$

In the case of bottom reflection,

$$z'_R = \tan(2\theta_B - \theta_I) \quad , \tag{II.25}$$

where $\theta_I = \tan^{-1}(z'_I)$ is the incident ray path angle and $\theta_B = \tan^{-1}(z'_B)$ is the ocean bottom slope angle.

B. Intensity in an Azimuthally Symmetrical Environment

As shown in the derivation of Eq. II.13 and in Fig. 1, the calculation of intensity depends upon the calculation of the infinitesimal areas of the wave front surfaces W_1 and W_2, which are swept out by making small variations in the ray launch angles. In the azimuthally symmetrical environment of Fig. 2, the area of W_2 at horizontal range r is given by

$$\text{area } W_2 = \left|(r\delta\psi_s)\ (\delta z \cos\theta)\right| = \left|(r\delta\psi_s)\ (\delta r \sin\theta)\right| \quad . \tag{II.26}$$

Since Eq. II.13 is an expression for intensity ratios, it is convenient to compute the ratio of the intensity at an arbitrary point along the ray path to a reference intensity measured one unit distance from the source. The area of the surface at unit distance from the source, W_1, is from Eq. II.26 and Fig. 2,

$$\text{area } W_1 = \left|\cos\theta_s \; \delta\psi_s \; \delta\theta_s\right| \quad . \tag{II.27}$$

Then, by Eqs. II.13, II.26, and II.27, the intensity ratio is

$$\frac{I_2}{I_1} = \left|\frac{\cos\theta_s}{r\cos\theta \; \delta z/\delta\theta_s}\right| = \left|\frac{\cos\theta_s}{r\sin\theta \; \delta r/\delta\theta_s}\right| \quad . \tag{II.28}$$

Passing to the limit of vanishing launch angle variations,

$$\frac{I_2}{I_1} = \left|\frac{\cos\theta_s}{r\,\frac{\partial z}{\partial\theta_s}\cos\theta}\right| = \left|\frac{\cos\theta_s}{r\,\frac{\partial r}{\partial\theta_s}\sin\theta}\right| \quad . \tag{II.29}$$

The calculation of intensity thus requires the calculation of either $\partial z/\partial\theta_s\big|_{r=\text{const}}$ or $\partial r/\partial\theta_s\big|_{z=\text{const}}$, the vertical and horizontal rates of ray spreading with changing launch depression angle.

The intensity ratio of Eq. II.29, when expressed in decibels, is the propagation loss, or transmission loss, due to geometrical spreading along the ray. A fuller treatment of propagation loss must await a discussion of eigenrays, and so is deferred to Chapter VII, where the role and implementation of propagation loss in ray models is described.

One can sometimes estimate $\partial z/\partial\theta_s$ by tracing two rays with slightly different launch angles out to range r, where the arrival depths will differ by δz for a launch angle difference of $\delta\theta_s$. One then makes the finite difference approximation $\partial z/\partial\theta_s \approx \delta z/\delta\theta_s$. Similarly, one might estimate $\partial r/\partial\theta_s$ by tracing two rays to a common depth and using $\partial r/\partial\theta_s \approx \delta r/\delta\theta_s$. Indeed, these procedures are used in ray models, but they are not very satisfactory. They can at best attain an error on the order of $\delta\theta_s^2$ and are subject to cancellation errors.[17]

Moreover, even a slight change in the ray launch angle may cause a ray to follow a path which suddenly veers from the course followed by the companion ray. For example, a slight change in the launch angle of a ray which passes near the surface of the ocean could cause the ray to strike the surface and reflect from it. The surface reflected ray and the surface grazing ray would not be suitable ray pairs for the finite difference method at any range beyond the surface reflection point because both $\partial z/\partial\theta_s$ and $\partial r/\partial\theta_s$ are discontinuous in the launch angle interval $(\theta_s, \theta_s+\delta\theta_s)$ beyond that range.

To avoid numerical differentiation, we seek a method of computing $\partial z/\partial\theta_s$ along a ray path as the ray trace progresses. Solomon and Armijo[18] proposed a suitable method, described below.

The ray path depth z at range r is a function not only of the range, but also of the ray launch angle, that is, $z=z(r,\theta_s)$. One may therefore differentiate the ray path equation (Eq. II.21) with respect to θ_s to obtain

$$\zeta'' = \left[\frac{2z'z''}{1+z'^2} - (1+z'^2)\frac{n_r}{n}\right]\zeta' + \left[(1+z'^2)\left(\frac{n_{zz}}{n} - z'\frac{n_{rz}}{n}\right) - z''\frac{n_z}{n}\right]\zeta \quad , \text{(II.30)}$$

where $\zeta = \partial z/\partial\theta_s$, $n_{zz} = \partial^2 n/\partial z^2$, $n_{rz} = \partial^2 r/\partial z \partial r$, and primes denote d/dr.

Initial values $\zeta(z_s)$ and $\zeta'(z_s)$ are needed to solve Eq. II.30. Since the source depth is given and does not depend on θ_s,

$$\zeta(z_s) = 0 \quad . \tag{II.31}$$

Since $z'(r) = \tan\theta$,

$$\zeta' = \frac{\partial z'}{\partial \theta_s} = \frac{\partial \theta}{\partial \theta_s} \sec^2\theta \tag{II.32}$$

so that, at the source,

$$\zeta'(z_s) = \sec^2\theta_s \quad . \tag{II.33}$$

When a ray reflects from the bottom, a new set of initial values for ζ and ζ' is needed in order to proceed with the solution of Eq. II.30. Figure 3 shows two rays, differing in launch angle by the small increment $\delta\theta_s$, striking the bottom at two slightly separated points, labeled 1 and 2. The value of ζ at the point of incidence is, by definition, the limit

$$\zeta_I = \lim_{\delta\theta_s \to 0} \frac{z_2 - z_4}{\delta\theta_s} \tag{II.34}$$

(see Fig. 3). Similarly, the value of ζ' at the point of incidence is

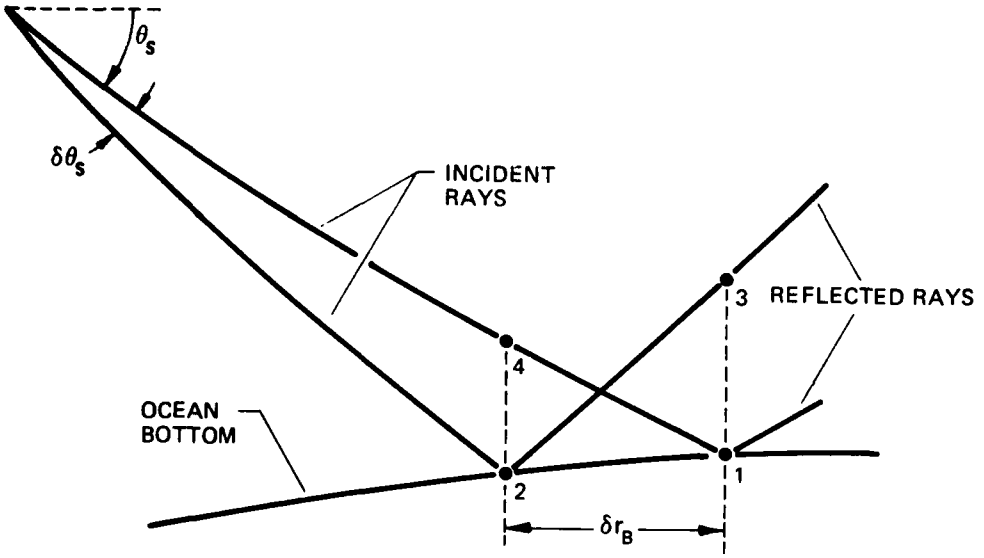

FIGURE 3
THE EFFECTS OF CHANGING LAUNCH ANGLE
ON BOTTOM REFLECTED RAYS

ARL:UT
AS-83-1188
TLF - GA
11-8-83

$$\zeta_I' = \lim_{\delta\theta_s \to 0} \frac{z_2' - z_4'}{\delta\theta_s} \quad . \tag{II.35}$$

Upon reflection, ζ and ζ' take on the new values

$$\zeta_R = \lim_{\delta\theta_s \to 0} \frac{z_3 - z_1}{\delta\theta_s} \tag{II.36}$$

and

$$\zeta_R' = \lim_{\delta\theta_s \to 0} \frac{z_3' - z_{R1}'}{\delta\theta_s} \quad . \tag{II.37}$$

where z_{R1}' is the ray path slope at point 1 upon reflection. We will now derive expressions for ζ_R and ζ_R' in terms of ζ_I, ζ_I', and the geometry of the ray path and bottom. The task is complicated by the fact that both the ray paths and the bathymetry are curvilinear.

The approach used will be to express the values of z, z', ζ, and ζ' at the points 2, 3, and 4 as first order Taylor series expansions about point 1 and substitute in Eqs. II.36 and II.37. The final expressions are exact, not first order approximations, because of the limiting process.

Let us begin with the derivation of ζ_R by deriving an expression for z_3 to first order in $\delta\theta_s$.

$$z_2 = z_1 + (r_2 - r_1) z'_{B1} + \ldots$$

$$= z_1 + \delta\theta_s \frac{\partial r_B}{\partial \theta_s} z'_{B1} + \ldots \quad , \tag{II.38}$$

$$z_3 = z_2 + (r_1 - r_2) z'_{R2} + \ldots$$

$$= z_1 + \delta\theta_s \frac{\partial r_B}{\partial \theta_s} z'_{B1} - \delta\theta_s \frac{\partial r_B}{\partial \theta_s} z'_{R2} + \ldots$$

$$= z_1 + \delta\theta_s \frac{\partial r_B}{\partial \theta_s} z'_{B1} - \delta\theta_s \frac{\partial r_B}{\partial \theta_s} (z'_{R1} + \ldots) + \ldots$$

$$= z_1 + \delta\theta_s \frac{\partial r_B}{\partial \theta_s} (z'_{B1} - z'_{R1}) + \ldots \quad , \tag{II.39}$$

where $\delta r_B = r_2 - r_1$, z'_{B1} is the bottom slope at point 1, z'_{R2} is the ray path slope upon reflection from point 2, and $\partial r_B / \partial \theta_s$ is the rate at which the range of the bottom intercept changes with launch angle. Note that in Eq. II.39, it is permissible to make the approximation $z'_{R2} \simeq z'_{R1}$ because only first order terms in $\delta\theta_s$ are being retained. Later, during the derivation of ζ'_R, the full first order expansion of z'_{R2} will be needed.

The quantity $\partial r_B / \partial \theta_s$ will be needed several times in the remainder of this section and also in Chapter V, so it is worthwhile to develop an expression for it here. Again, to first order,

$$z_2 = z_1 + \delta r_B z'_{B1} + \ldots \quad . \tag{II.40}$$

But another expansion for z_2 is also available:

$$z_4 = z_1 + \delta r_B z_1' + \ldots \quad , \tag{II.41}$$

$$z_2 = z_4 + \delta\theta_s \zeta_4 + \ldots$$

$$= z_1 + \delta r_B z_1' + \delta\theta_s(\zeta_1 + \ldots) + \ldots$$

$$= z_1 + \delta r_B z_1' + \delta\theta_s \zeta_1 + \ldots \quad . \tag{II.42}$$

Combining Eqs. II.40 and II.42 and taking the limit $\delta\theta_s \to 0$ yields

$$\frac{\partial r_B}{\partial \theta_s} = \lim_{\delta\theta_s \to 0} \frac{\delta r_B}{\delta \theta_s}$$

$$= \zeta \frac{1}{z_B' - z_I'} \quad . \tag{II.43}$$

Notice the use of the first order approximation $\zeta_1 = \zeta_4$ in Eq. II.42.

With z_3 and $\partial r_B / \partial \theta_s$ now in hand, it is possible to evaluate the right-hand side of Eq. II.36 to obtain

$$\zeta_R = -\zeta_I \frac{z'_B - z'_R}{z'_B - z'_I} \quad . \tag{II.44}$$

If desired, Eq. II.44 can be rewritten with the aid of trigonometric identities in the form

$$\zeta_R = -\zeta_I \frac{\cos\theta_I}{\cos\theta_R} \quad . \tag{II.45}$$

Turning now to ζ'_R, we see from Eq. II.37 that a first order expansion of z'_3 is needed.

$$\begin{aligned} z'_3 &= z'_{R2} + (r_1 - r_2) z''_{R2} + \ldots \\ &= z'_{R2} - \delta\theta_s \frac{\partial r_B}{\partial \theta_s} (z''_{R1} + \ldots) + \ldots \\ &= z'_{R2} - \delta\theta_s \frac{\partial r_B}{\partial \theta_s} z''_{R1} + \ldots \quad . \end{aligned} \tag{II.46}$$

Here, we are able to make the approximation $z''_{R2} \simeq z''_{R1}$, but this time we must develop the first order expansion of z'_{R2}.

$$\begin{aligned} z'_4 &= z'_1 + (r_2 - r_1) z''_1 + \ldots \\ &= z'_1 + \delta\theta_s \frac{\partial r_B}{\partial \theta_s} z''_1 + \ldots \quad , \end{aligned} \tag{II.47}$$

$$z_2' = z_4' + \delta\theta_s \zeta_4' + \ldots$$

$$= z_1' + \delta\theta_s \frac{\partial r_B}{\partial \theta_s} z_1'' + \delta\theta_s(\zeta_1' + \ldots) + \ldots$$

$$= z_1' + \delta\theta_s\left(\frac{\partial r_B}{\partial \theta_s} z_1'' + \zeta_1'\right) + \ldots \quad , \tag{II.48}$$

$$z_{B2}' = z_{B1}' + (r_2 - r_1) z_{B1}'' + \ldots$$

$$= z_{B1}' + \delta\theta_s \frac{\partial r_B}{\partial \theta_s} z_{B1}'' + \ldots \quad , \tag{II.49}$$

$$z_{R2}' = \tan(2\theta_{B2} - \theta_2)$$

$$= \tan\left(2\tan^{-1}(z_{B2}') - \tan^{-1}(z_2')\right)$$

$$= \tan\left(2\tan^{-1}\left(z_{B1}' + \delta\theta_s \frac{\partial r_B}{\partial \theta_s} z_{B1}'' + \ldots\right)\right.$$

$$\left. - \tan^{-1}\left(z_1' + \delta\theta_s\left(\frac{\partial r_B}{\partial \theta_s} z_1'' + \zeta_1'\right) + \ldots\right)\right) \quad . \tag{II.50}$$

Using

$$\tan(x+\varepsilon) = \tan x + \varepsilon \sec^2 x + \ldots \quad , \tag{II.51}$$

$$\tan^{-1}(x+\varepsilon) = \tan^{-1} x + \varepsilon \frac{1}{1 + x^2} + \ldots \tag{II.52}$$

and retaining only terms up to first order in $\delta\theta_s$, Eq. II.50 becomes

$$z'_{R2} = z'_{R1} + \delta\theta_s \left(2\zeta_1 \frac{z''_{B1}}{z'_{B1} - z'_1} \frac{\cos^2\theta_{B1}}{\cos^2\theta_{R1}} - \zeta_1 \frac{z''_1}{z'_{B1} - z'_1} \frac{\cos^2\theta_1}{\cos^2\theta_{R1}} - \zeta'_1 \frac{\cos^2\theta_1}{\cos^2\theta_{R1}} \right) \quad . \tag{II.53}$$

We may now evaluate the right-hand side of Eq. II.37, using Eqs. II.43, II.46, and II.53, to obtain

$$\zeta'_R = 2\zeta_I \frac{z''_B}{z'_B - z'_I} \frac{\cos^2\theta_B}{\cos^2\theta_R} - \zeta_I \frac{z''_I}{z'_B - z'_I} \frac{\cos^2\theta_I}{\cos^2\theta_R} - \zeta_I \frac{z''_R}{z'_B - z'_I} - \zeta'_I \frac{\cos^2\theta_I}{\cos^2\theta_R} \quad . \tag{II.54}$$

New values for ζ and ζ' are also required when a ray reflects from the surface. Derivation of expressions for ζ_R and ζ'_R proceeds in the same way as for bottom reflections, but is very much simplified by the assumption that the surface, unlike the bottom, is horizontal and perfectly flat. The results are

$$\zeta_R = -\zeta_I \tag{II.55}$$

and

$$\zeta'_R = \zeta_I \frac{z''_I}{z'_I} + \zeta_I \frac{z''_R}{z'_I} - \zeta'_I \quad . \tag{II.56}$$

C. Summary

In this chapter expressions involving differential equations have been derived for ray paths and intensities in azimuthally symmetrical ocean environments. Also derived were initial values needed to start the solutions of the differential equations at the source and to restart the solutions when rays reflect from the surface and bottom.

III. SOLUTION OF THE RAY EQUATIONS

In this section we will discuss methods for solving the ray path equation (Eq. II.21) and the depth spreading equation (Eq. II.30), which are practical for implementation on a digital computer. Since the computational effort expended tracing rays typically exceeds by two orders of magnitude the efforts required in any other single computational task, and since the success of any attempt to locate eigenrays or perform any other further processing depends critically on high quality ray traces, the ray tracing techniques may be the single most important facet of a ray model.

Ray trace methods based on analytical solutions of the ray equations are discussed in the section below. Models which rely entirely on these methods have generally not been very successful. The difficulties with analytical methods are set forth in some detail not only because they are frequently employed, but also because hybrid analytical/numerical techniques show promise of substantially improving future ray tracing techniques. Hybrid methods employ numerical perturbation procedures to refine approximate analytical computations, but the analytical expressions used must be extricated from the pitfalls described below.

The numerical ray tracing methods currently employed in MEDUSA are discussed in Section III.B.

A. Analytic Solution of the Ray Equations

One can sometimes solve the ray path equation, the depth spreading equation, and even the equations of intersection of rays with boundaries, when $n(r,z)$ and the bathymetry are particularly simple functions. For example, if $\vec{\nabla}(1/n)$ is a constant vector, then the ray paths can be shown to be circular arcs.

Furthermore, one can approximate more complicated n's to any desired degree of accuracy by breaking up the r-z plane into a patchwork of smaller domains and fitting $n(r,z)$ in each domain with simple (tractable) functions. The ray paths are then constructed by solving the ray path equation analytically within each domain traversed and connecting the path segments. One could, for example, break up the r-z plane into triangles within which the ray paths are circular arcs.

The availability of analytic solutions to the ray equations makes this procedure seem attractive; and it is, in fact, used in a number of ray models. However, the method suffers from several drawbacks, which are examined below.

Perhaps the most serious difficulty has to do with seemingly innocuous limitations of the fitting functions used to approximate n. When n is approximated with some of the simplest and most convenient fitting functions, such as the one which gives circular ray arcs, the resulting gradients n_z and n_r are generally mismatched at the boundaries of the small domains. These discontinuities in turn give rise to discontinuities in $z(r,\theta_s)|_{r=\text{const}}$. (Recall that the derivative of this function with respect to θ_s is the depth spreading function ζ.) In other words, if the fitting functions do not preserve the smoothness of n, then the ray paths do not change smoothly with changing launch angle. These erratic ray paths produce well publicized anomalies in propagation loss curves,[19] such as false caustics and shadow zones; but more importantly, they greatly complicate the process of locating the eigenrays (rays connecting the source and receiver) which are needed to compute propagation loss. Location of eigenrays and the ramifications of discontinuities are discussed in Chapter V.

One might solve this problem by finding fitting functions which are flexible enough to permit the gradients of n to be matched at the domain boundaries, but the author is not aware of any such functions which do not introduce nonphysical contortions in n and yet are still

simple enough in form to allow solution of the ray equations. And even if such functions could be found, it turns out that even discontinuities in the second derivatives of n can cause anomalies in propagation loss calculations.

One might also mitigate the problem by creating smaller and more numerous domains, with smaller gradient mismatches, in order to better approximate n, but this may impose unacceptable demands on computer resources. Yet, experience shows that ray model predictions are often sensitive to the number and location of domains, an indication that the number of domains typically used is too small to produce stable, reliable predictions.

A second set of difficulties relates to the analytic solutions to the ray equations. It is sometimes assumed that solutions of the path equations in the form of combinations of algebraic or elementary transcendental functions automatically guarantees accurate computation since these simple functions are readily available on computers and can be evaluated with great accuracy. This is not at all the case; the solutions to the ray equations usually will have to be recast in mathematically equivalent forms which are resistant to cancellation errors and other numerical difficulties. To do this requires specialized knowledge of numerical analysis and is something of an art in any case. It is also necessary to ensure that the ray formulas do not break down for certain limiting cases. The author knows of several ray models which fail when n is a constant.

Lastly, analytic solutions of the ray equations are inherently dependent on the form of the function n. If n is changed, then new solutions to the path equations must be derived. For example, if a ray model were developed in which $\vec{\nabla}(1/n)$ was a constant vector, then the corresponding ray paths would be circular arcs. If, later on, one wished to change n(r,z) so that $\vec{\nabla}(n^2)$ was a constant vector instead, then one would also have to revise the part of the model concerned with tracing

rays so that the circular arcs become parabolic arcs. The depth spreading formulas, boundary intersection formulas (if any), travel time formulas, path length formulas, and any other ray formulas would also have to be altered. The necessary modifications to the model clearly could be very extensive, yet the ability to change n readily is a very valuable asset to a ray model, particularly if the model is intended to be a research tool.

B. Numerical Solution of the Ray Equations

All of the foregoing difficulties are avoided (or at least exchanged for a different set of problems) if the ray equations are solved numerically.

Methods for solving ordinary differential equations have been the subject of vigorous research within the field of numerical analysis for several decades and a great many procedures have been developed. It will therefore not be necessary to develop any new techniques, but rather to identify the methods best suited to solving the ray equations. As we shall see, the methods of choice turn out to be some of the oldest and simplest.

The most outstanding fact about ray traces from the standpoint of computational procedure is that the progress of a ray is highly eventful. It may undergo surface reflections and bottom reflections, it may pass through caustics (points where $\zeta=0$ and the ray theory approximation $K \approx k$ breaks down), it can encounter receivers, it may pass through turning points (where $z'=0$), and so on. It is essential to diagnose these events as they occur, locate them precisely and, in the case of boundary reflections, restart the ray trace with new initial conditions. This at once removes from consideration various global methods for solving differential equations which rely on variational principles and which are not well suited to discovering and responding to local disruptions.

We shall therefore restrict our attention to incremental methods, which will allow us to advance the solution to the ray path equation in a series of small range steps leading away from the source. After each tentative step, an exhaustive battery of tests will be performed to locate any significant events which may have occurred within the range step. In response to some events, such as boundary encounters, it will be necessary to reject the step and adjust the range step size so that the ray path segment ends exactly where the event occurs in order to reinitialize and properly resume the ray trace after the event.

In addition, it has proven highly advantageous to be able to vary the step size in response to changes in the environment. In order to maintain desired accuracy in the ray trace, a step size of no more than a few meters may be possible as a ray undergoes rapid undulations near the surface, where n_z may vary rapidly. Yet, step sizes of a kilometer or more may be permissible for the same ray as it travels in deep water, where n_z is nearly constant.

The search has now been narrowed to methods which are easily started (and restarted) and permit the step size to vary continuously. These requirements unfortunately rule out the multistep and variable order methods which have occupied much of the attention of numerical analysts in recent years. When applicable, these methods can be extremely accurate and efficient, but they require somewhat complicated and inconvenient initialization procedures, they can only double or halve their step sizes conveniently, and they lose efficiency when interrupted after every step. We are left with Runge-Kutta methods[20] and Taylor series expansions.

In fact, we are confined to Runge-Kutta and Taylor series methods of low order. The Taylor series expansion for the ray path depth z at range $r+\Delta r$, given the path depth and its range derivatives at range r, is

$$z(r+\Delta r) = z(r) + \Delta r z'(r) + \frac{1}{2}\Delta r^2 z''(r) + \frac{1}{6}\Delta r^3 z'''(r) + \ldots \quad . \tag{III.1}$$

The accuracy of the expansion is limited by the number of continuous derivatives of z there are in the interval $(r,r+\Delta r)$; accuracy increases as more terms are added until a term with a discontinuous derivative is encountered. The order of the expansion is given by the largest power of Δr included in the series. Runge-Kutta methods do not depend explicitly on the derivatives as Taylor series do, but they are derived from Taylor series expansions and are subject to exactly the same accuracy limitations. The order of a given Runge-Kutta method is the same as the order of the Taylor series it was derived from. Repeated differentiation of the ray path equation,

$$z'' = (1+z'^2)\left(\frac{n_z}{n} - z'\frac{n_r}{n}\right) \quad ,$$

shows that the higher derivatives of z remain continuous only as long as the gradients of n remain continuous. A practical method is developed in Chapter IV which achieves two continuous gradients of n at domain boundaries (all gradients are continuous within the domains). With that limitation, experience indicates that greatest efficiency is achieved with methods of about order three. Higher order methods lose efficiency crossing domain boundaries, where their greater computational costs are not offset by increased accuracy and the ability to take longer range steps.

Taylor series methods are effectively limited to second order because of the inconvenience of computing higher derivatives of z and ζ. Therefore, the method currently implemented in MEDUSA is a third order Runge-Kutta method, specifically, Kutta's third order rule.[21] Using this

method, the ray path depth and ray path slope at $r+\Delta r$ are computed from $z(r)$ and $z'(r)$ by application of the formulas

$$\begin{bmatrix} z(r+\Delta r) \\ z'(r+\Delta r) \end{bmatrix} = \begin{bmatrix} z(r) \\ z'(r) \end{bmatrix} + \frac{\Delta r}{6} \begin{bmatrix} z'(r) + 4z_1' + z_2' \\ z''(r) + 4z_1'' + z_2'' \end{bmatrix} , \quad \text{(III.2)}$$

$$\begin{bmatrix} r_1 \\ z_1 \\ z_1' \\ z_1'' \end{bmatrix} = \begin{bmatrix} r + \frac{\Delta r}{2} \\ z(r) + \frac{\Delta r}{2} z'(r) \\ z'(r) + \frac{\Delta r}{2} z''\left(r, z(r), z'(r)\right) \\ z''(r_1, z_1, z_1') \end{bmatrix} , \quad \text{(III.3)}$$

$$\begin{bmatrix} r_2 \\ z_2 \\ z_2' \\ z_2'' \end{bmatrix} = \begin{bmatrix} r + \Delta r \\ z(r) + \Delta r\left[2z_1' - z'(r)\right] \\ z'(r) + \Delta r\left[2z_1'' - z''\left(r, z(r), z'(r)\right)\right] \\ z''(r_2, z_2, z_2') \end{bmatrix} , \quad \text{(III.4)}$$

$$z''(r,z,z') = (1+z'^2)\left(\frac{n_z(r,z)}{n(r,z)} - z'\frac{n_r(r,z)}{n(r,z)}\right) . \quad \text{(III.5)}$$

This simple Runge-Kutta formula lacks a procedure for estimating the error incurred in taking a step. One independent means of

estimating the error is based on a recasting of the ray path equation in the form of an integro-differential equation:

$$n_1^2 \cos^2\theta_1 = n_0^2 \cos^2\theta_0 + \int_{r_0}^{r_1} \frac{\partial(n^2)}{\partial r}\, dr \quad . \qquad \text{(III.6)}$$

Equation III.6 is a generalized form of Snell's law which is applicable when n is a function of range as well as depth. In a horizontally stratified (range independent) medium, $n_r=0$ and Eq. III.6 reduces to Snell's law: $n_1^2\cos\theta_1 = n_0^2\cos^2\theta_0$. One can differentiate Eq. III.6 with respect to r and recover the ray path equation. If one lets $r_0=r$ and $r_1=r+\Delta r$, takes a step using Eqs. III.2-5, and then evaluates the left- and right-hand sides of Eq. III.6, then the inevitable discrepancy between the left- and right-hand side is a measure of the numerical error incurred in the step. This procedure does not yield error estimates for the ray path depth and slope; it is a measure of how well the predicted and actual values of $n_1^2\cos^2\theta_1$ agree.

The error incurred in one step using Kutta's third order rule is roughly proportional to Δr^4. If the estimated error in a step is unacceptably large, then the step is rejected and attempted anew using a step size reduced in accordance with the fourth power law. On the other hand, if the error is much smaller than allowable, one can increase the step size for the next step, again using the fourth power law as a guide.

The efficacy of Kutta's third order rule, together with the error estimator, has been severely tested by comparing solutions obtained using these methods with known solutions for analytically tractable forms of n. Not only do the rays arrive within a few millimeters of the correct depths across range intervals of thousands of kilometers, but the errors themselves are usually very close to the specified tolerances. Kutta's third order rule is also used to solve the depth spreading equation.

The error estimation procedure calls for the numerical evaluation of a definite integral. The integrity of the error estimation procedure requires a numerical integrator of higher order than Kutta's third order rule, so that the integrator itself does not become an important source of error. A suitable integrator is the Euler-Maclaurin formula[22]

$$\int_{x_0}^{x_1} f(x)dx = \frac{(x_1-x_0)}{2}\left[f(x_0)+f(x_1)\right] - \frac{(x_1-x_0)^2}{12}\left[f'(x_1)-f'(x_0)\right] + \frac{(x_1-x_0)^5}{720} f^{(4)}(\nu) \quad , \tag{III.7}$$

$$x_0 \leq \nu \leq x_1 \quad .$$

The error term $(x_1-x_0)^5 f^{(4)}(\nu)/720$ compares favorably with the error term of the more familiar Simpson's rule[23] integrator. The Simpson's rule error term is $(x_1-x_0)^5 f^{(4)}(\nu)/90$.

The Euler-Maclaurin integrator requires not only the values of the integrand at x_0 and x_1, but also the values of the derivative of the integrand. Thus, inspection of Eq. III.6 reveals that the range derivative of $\partial(n^2)/\partial r$ is needed. It is

$$\frac{d}{dr}\frac{\partial(n^2)}{\partial r} = \left(\frac{\partial}{\partial r} + z'\frac{\partial}{\partial z}\right)\frac{\partial(n^2)}{\partial r} = 2\left[n_r^2 + nn_{rr} + z'(n_z n_r + nn_{rz})\right] \quad . \tag{III.8}$$

The author has also experimented with Runge-Kutta-Fehlberg methods[24] for solving the ray equations. They proved successful, offering the ability to estimate errors and readily adjust the step size to accommodate error tolerances and variations in the environment, but their greater complexity and a tendency to balk at domain interfaces made them less advantageous than the procedure described earlier. Runge-Kutta-Fehlberg methods are general purpose algorithms and, as such, cannot make use of specialized information about the differential equations they may be required to solve, as we have done here.

It is expected that further research into ray tracing techniques will be carried out. The present method is more than sufficiently accurate, but it is somewhat slow.

C. Path Length and Travel Time Integrals

The integrals for path length and travel time are

$$s = \int_0^r (1+z'^2)^{1/2}\, dr \qquad \text{(III.9)}$$

and

$$t = \frac{1}{c_0} \int_0^r n(1+z'^2)^{1/2}\, dr \quad . \qquad \text{(III.10)}$$

The most popular numerical method for computing such integrals, Simpson's rule, is inappropriate here because the range points at which the

integrands are available are neither equally spaced nor necessarily odd in number, as required by Simpson's rule. However, at each end of a range step one has available the integrands and their range derivatives at both ends of a given range step:

$$\frac{ds}{dr} = (1+z'^2)^{1/2} = \sec\theta \quad , \tag{III.11}$$

$$\frac{d^2s}{dr^2} = z'z''\cos\theta \quad , \tag{III.12}$$

$$\frac{dt}{dr} = \frac{n}{c_0}\frac{ds}{dr} \quad , \tag{III.13}$$

and

$$\frac{d^2t}{dr^2} = \frac{n}{c_0}\left[\left(\frac{n_r}{n} + z'\frac{n_z}{n}\right)\frac{ds}{dr} + \frac{d^2s}{dr^2}\right] \quad . \tag{III.14}$$

The third order Euler-Maclaurin formula is used to compute the contributions to the integrals over a range step using the integrands and their range derivatives.

D. Summary

In this chapter the ray path and intensity differential equations were cast in forms suitable for solution on a digital computer. The numerical procedure used, Kutta's third order rule, was described and the reasons for selecting it were presented. An expression for the ray

path error tolerance was derived and the numerical method for achieving the accuracy requirement by varying the integration step size was presented. Lastly, the use of the Euler-Maclaurin formula to perform the ray path length and travel time integrations was explained.

IV. REPRESENTATION OF THE BATHYMETRY AND SOUND SPEED

Bathymetry is usually presented to ray models in the form of a table of measured ocean bottom depths as a function of range from the source. To simplify location of eigenrays, it is necessary to fit the tabular data with a function which provides two continuous derivatives of the depth with respect to range. There is a function which is designed to do just that; it is called a cubic spline.[25] The use of cubic splines to fit sound speed profile data in range invariant environments was suggested by Moler and Solomon.[26] The ray model GRASS[13] fitted splines to profiles in range dependent environments and traced rays numerically.

A. Cubic Splines

The cubic spline is usually defined to have the following properties:

(1) Given tabular data x_i, y_i, where the x_i's are abscissas, the y_i's are the corresponding ordinates, and $1 \le i \le n$, the cubic spline $S(x)$ is defined to be the union of cubic polynomials $S_i(x)$. Each S_i is defined on the interval $x_i \le x \le x_{i+1}$.

(2) $S_i(x_i) = y_i$.

(3) $S_i'(x_i) = S_{i-1}'(x_i)$.

(4) $S_i''(x_i) = S_{i-1}''(x_i)$.

(5) $S_1''(x_1) = S_{n-1}(x_n) = 0$.

It can be shown that the cubic spline, thus defined, is unique. It can also be shown that

$$\delta \int_{x_1}^{x_n} \left[S''(x)\right]^2 dx = 0 \quad , \qquad \text{(IV.1)}$$

that is, the cubic spline is the function which minimizes a quantity closely related to the total curvature of a curve, subject to the constraints that the spline interpolates the data and has two continuous derivatives.

Cubic splines perform very well when the data are well sampled, but bathymetric data are often very sketchy. When cubic splines were used to fit undersampled bathymetry data, the result was often something like that depicted in Fig. 4. The four data points were intended to represent the transition from an abyssal plain through a continental slope to a continental shelf, as indicated by the linear segments. When the data are fitted with a cubic spline, however, the spline is seen to undergo unintended excursions, resulting in a nonphysical basin and in the creation of an "island". These anomalous features, hereafter called spline artifacts, are a consequence of the spline's extremalizing property.

The detection and correction of spline artifacts proved to be an extremely onerous process, involving the repeated generation of high resolution plots of suspect portions of the bathymetry and the painstaking insertion of corrective data points into the bathymetric data.

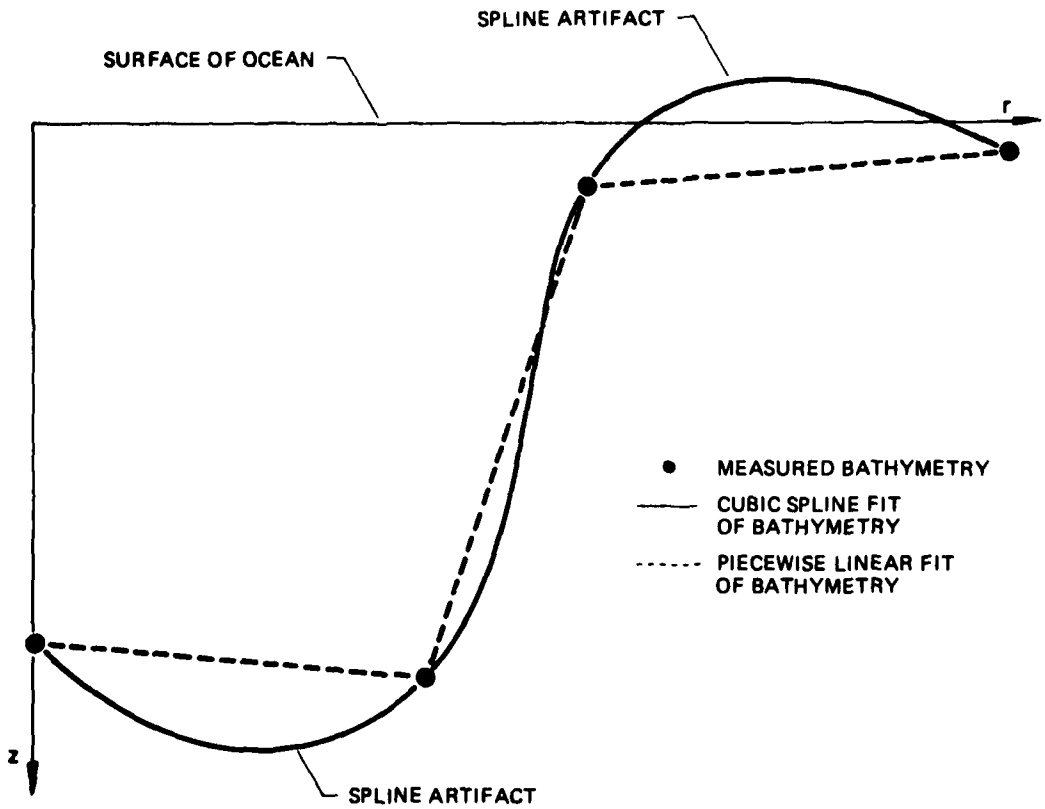

FIGURE 4
CUBIC SPLINE ARTIFACTS IN BATHYMETRY

ARL:UT
AS-83-1189
TLF-GA
11-8-83

The problem of spline artifacts was solved by inventing a new spline fitting procedure. The new fitting function, described below, will be referred to as a T-spline.

B. T-Splines

The rationale for the development to follow is that, to be consonant with the spline user's expectations, the T-spline should be linear over most of the region between the data points; nevertheless, the T-spline $T(x)$ is to be everywhere continuous through the second derivative. The extremalizing condition is counterproductive here and will not be retained. The requirement that $T(x)$ interpolate the data will be slightly relaxed, a concession to the requirement that $T(x)$ be twice differentiable everywhere.

To proceed with the definition of the T-spline, we introduce new abscissa values $x_{i,0}$ and $x_{i,1}$ to either side of the original abscissa values x_i for $2 \le i \le n-1$ (that is, for every x_i except the first one and the last one) as follows:

$$x_{i,0} = x_i - \Delta x \qquad \text{(IV.2)}$$

and

$$x_{i,1} = x_i + \Delta x \quad , \qquad \text{(IV.3)}$$

where the increment Δx is always chosen small enough that

$$\Delta x < \frac{1}{2} (x_i - x_{i-1}) \qquad \text{(IV.4a)}$$

and

$$\Delta x < \frac{1}{2}(x_{i+1}-x_i) \qquad \text{(IV.4b)}$$

(see Fig. 4). For each of these new abscissa values, we also introduce new ordinate values $y_{i,0}$ and $y_{i,1}$. The point $(x_{i,0},y_{i,0})$ is required to lie on the line segment connecting (x_{i-1},y_{i-1}) to (x_i,y_i). The point $(x_{i,1},y_{i,1})$ is required to lie on the line segment connecting (x_i,y_i) to (x_{i+1},y_{i+1}). The T-spline is the union of cubic polynomials defined below.

$$T(x) = a_0 + a_1\tau + a_2\tau^2 + a_3\tau^3 \quad ,$$

When $x_{i-1,1} \le x \le x_{i,0}$

$a_0 = y_{i-1,1}$,
$a_1 = (y_i-y_{i-1})/(x_i-x_{i-1})$,
$a_2 = 0$,
$a_3 = 0$, and
$\tau = x - x_{i-1,1}$.
T(x) is linear in this interval; the cubic polynomial is degenerate.

When $x_{i,0} \le x \le x_i$

$a_0 = y_{i,0}$,
$a_1 = (y_i-y_{i-1})/(x_i-x_{i-1})$,
$a_2 = 0$
$a_3 = (y_{i,0}-2y_i+y_{i,1})/(6\Delta x^3)$, and
$\tau = x - x_{i,0}$.

When $x_i \le x \le x_{i,1}$

$$a_0 = (y_{i,0}+4y_i+y_{i,1})/6,$$
$$a_1 = (y_{i,1}-y_{i,0})/(2\Delta x),$$
$$a_2 = (y_{i,0}-2y_i+y_{i,1})/(2\Delta x^2),$$
$$a_3 = -(y_{i,0}-2y_i+y_{i,1})/(6\Delta x^3), \text{ and}$$
$$\tau = x - x_i.$$

When $x_{i,1} \le x \le x_{i+1,0}$

$$a_0 = y_{i,1},$$
$$a_1 = (y_{i+1}-y_i)/(x_{i+1}-x_i),$$
$$a_2 = 0,$$
$$a_3 = 0, \text{ and}$$
$$\tau = x - x_{i,1} \quad .$$

T(x) is linear in this interval also.

It is straightforward, although tedious, to verify that T(x), thus defined, is continuous and everywhere twice differentiable. One can also show that $T(x_i) \neq y_i$, that is, T(x) does not interpolate the data.

C. T-Splines and the Bathymetry

Figure 5 shows that when the bathymetry data of Fig. 4 are fitted with a T-spline, the "corners" formed by connecting the bathymetry data with straight line segments are "rounded off" by the T-spline. But, for practical bathymetries, this rounding error has always proven to be on the order of a fraction of a meter, well below the limits of measurement error.

D. T-Splines and Sound Speed Profiles

In general, sound speed information is supplied to a ray model in the form of a series of sound speed profiles (sound speeds as

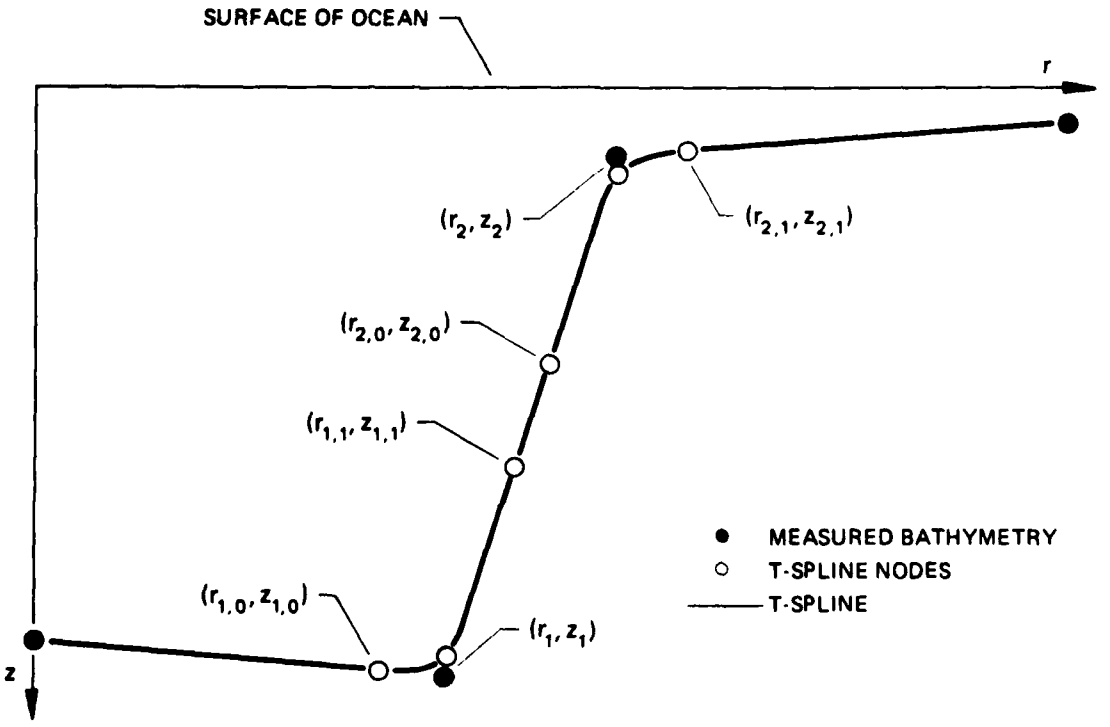

FIGURE 5
T-SPLINE FIT TO BATHYMETRY

ARL:UT
AS-83-1190
TLF-GA
11-8-83

functions of depth at given ranges) taken at various distances from the source. The requirement that $n(r,z)$ and several of its gradients be continuous can be met by fitting each sound speed profile separately with T-splines, which provides two continuous depth derivatives (n_z and n_{zz}) and performing linear interpolations in range between profiles to obtain continuous range derivatives (n_r and n_{rz}) between profiles.

The domains thus formed are rectangular, except where the bottom cuts through some of the rectangles to form its own, irregularly shaped domain boundaries. Except along the bottom, the boundaries of the rectangles are set by horizontal lines at the T-spline node depths and by vertical lines at the sound speed profile ranges.

V. EIGENRAYS

In principle, it is possible to locate an eigenray (a ray which connects a source and a receiver) by numerically searching between two rays which arrive at the receiver range above and below the receiver depth. In practice, it is not usually feasible to perform the numerical search because of the large number of rays which would have to be traced. Instead, one can interpolate between pairs of rays to locate eigenrays. Also, pairs of rays suitable for interpolation are usually not available for receivers near the surface because it is unlikely that a ray will pass through the small depth interval above the receiver and below the surface, even if a very large number of rays are traced. On the other hand, it is relatively easy with a large sample of rays to locate pairs of rays which bracket the receiver in range, so it is preferable to locate eigenrays by interpolating between rays which bracket the receiver in range, not depth.

The following strategy was adopted in MEDUSA for finding eigenrays. First, a large number of rays are traced in small increments of the launch angle from the source to a range beyond the range of the most distant receiver. As a ray progresses, it will undergo a series of significant events, such as surface reflections, transition through caustics, etc. These events, their order of occurrence, and certain path information associated with each event, together constitute the ray path history. Detailed ray path histories are recorded, including ranges at which rays cross a receiver depth. After this ray sweep-out is completed, eigenrays are located by scanning the ray history records for pairs of rays in which the sequence of events in the ray path histories are identical, but which differ by the launch angle increment and which bracket the receiver in range as they cross the receiver depth. A third order interpolation scheme is used to determine the eigenray launch angle. Other third order interpolations, together with the eigenray launch angle and information stored in the history records, then yield

arrival angles, travel times, and path lengths, as well as the locations of bottom reflection points and bottom grazing angles. A second order interpolation produces eigenray intensity. The details of the procedure are described in Section V.A, "Location of Eigenrays," and Section V.B, "Eigenray Path Data Interpolation."

This method of locating eigenrays offers several advantages in efficiency and reliability. The reliance on interpolation reduces the number of rays to be traced by eliminating the ray traces which would be required to probe numerically for eigenrays. Comparison of detailed ray path histories prevents attempting meaningless interpolations between rays which follow significantly different paths (for example, rays having different numbers of bottom reflections). Extrapolations are strictly avoided. The ray sweep-out approach makes it possible for rays, which may cross the receiver depth many times before the traces are terminated, to be used in many different eigenray interpolations for receivers at different ranges. Ray sweep-outs of several hundred rays have been used to locate thousands of eigenrays.

A. Location of Eigenrays

The procedure by which eigenrays are located using the ray history records lends itself to graphical illustration. Let the function $r(\theta_s)$ be the range at which a ray, with launch angle θ_s, crosses the receiver depth. This function will generally be multivalued since a ray may cross the receiver depth several times at different ranges. For example, Fig. 6 shows $r(\theta_s)$ for the sound speed profile and source and receiver shown in Fig. 7. The eigenray launch angles for a receiver located at range r_R are the zeroes of $r(\theta_s)-r_R$, as illustrated in Fig. 6 for r_R = 50 km.

Devising an automatic procedure for locating the zeroes accurately, reliably, and efficiently while avoiding false predictions is a challenging task. As Fig. 6 suggests, the range function $r(\theta_s)-r_R$ is

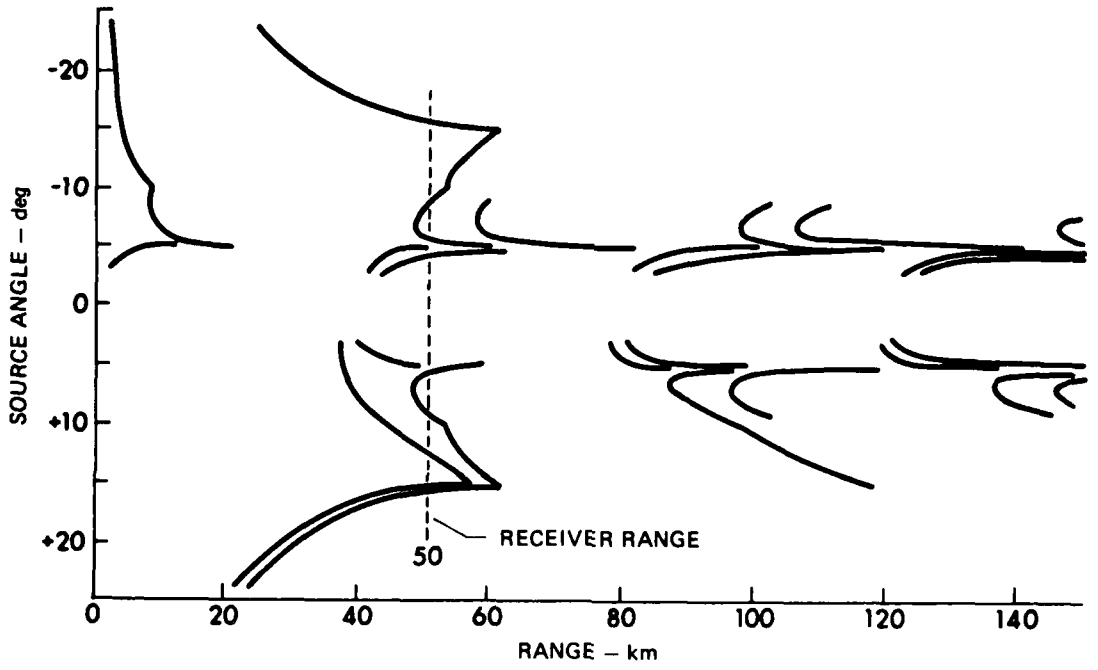

FIGURE 6
$r(\theta_s)$ DIAGRAM
SOURCE: 490 m
RECEIVER: 470 m

ARL:UT
AS-82-1668
TLF-GA
10-19-82

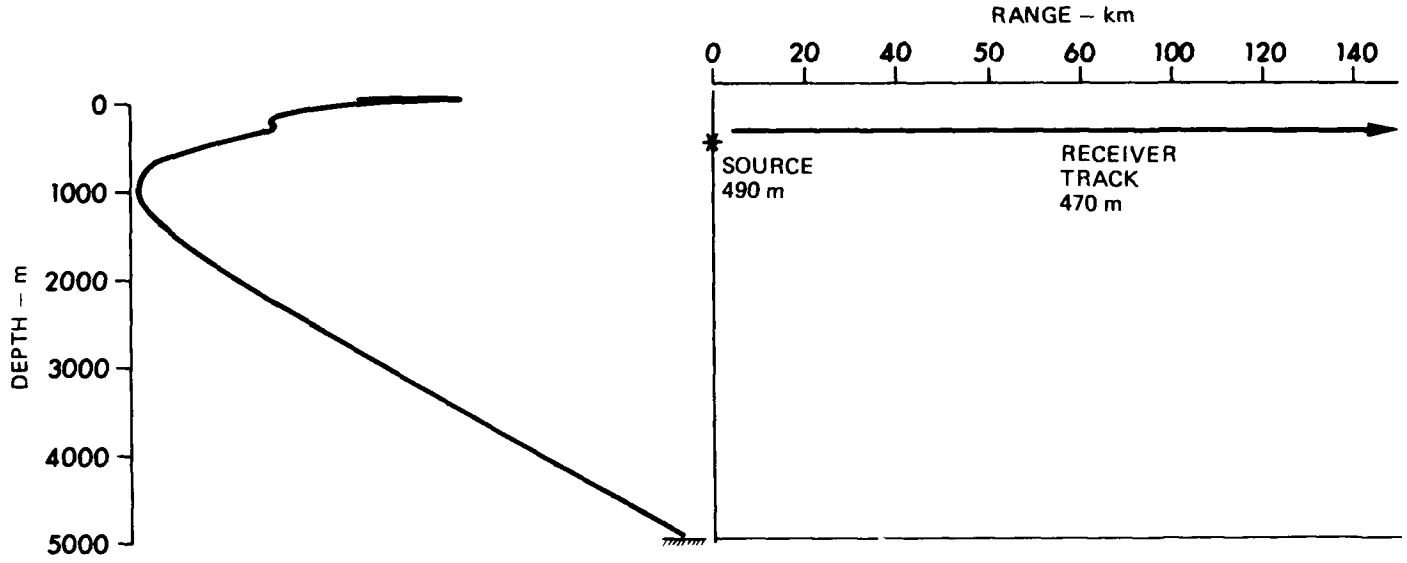

FIGURE 7
SOUND SPEED PROFILE AND SOURCE/RECEIVER CONFIGURATION
(RANGE INVARIANT ENVIRONMENT)

ARL:UT
AS-82-1669
TLF-GA
10-19-82

usually a complicated multivalued function having singularities, slope discontinuities, and an unknown number of zeroes. In fact, Fig. 6 provides a comparatively simple illustrative example; a more typical range function will be discussed in Section VII (see Fig. 13). A practical eigenray location scheme must determine the approximate locations of the zeroes, and it must refine the launch angle estimates to an acceptible degree of precision.

During the ray sweep-out, $r(\theta_s)$ is sampled at finely spaced intervals of θ_s. If the sampled points are designated by θ_{si} and r_i, then, with some restrictions, the zeroes are located in those intervals where

$$(r_i - r_R)\,(r_{i+1} - r_R) \leq 0 \quad .$$

It is impractical to locate an eigenray numerically by tracing trial rays in the interval $[\theta_{si}, \theta_{si+1}]$ because of the time needed to compute the individual rays and the large number of eigenrays to be found. Instead, $r(\theta_s)$ is replaced in the interval by a hermite cubic interpolating polynomial[27] $r_c(\theta_s)$, described below in Section V.A.1, and the zero of $r_c(\theta_s) - r_R$ is located numerically.

As we shall see, if hermite splines are to be substituted for $r(\theta_s)$, then we will need not only the values r_i for each of the θ_{si}, but also the values of $(\partial r/\partial\theta|_{z=z_R})_i$; that is, we need both r as a function of θ_s and the derivative of r with respect to θ_s at each of the θ_{si}. The quantity $\partial r/\partial\theta_s|_{z=\text{const}}$ was first encountered in Chapter II in connection with the calculation of intensity; it is the range spreading with changing launch angle. We define $\xi = \partial r/\partial\theta_s|_{z=\text{const}}$, much as we defined $\zeta = \partial z/\partial\theta_s|_{r=\text{const}}$ (the depth spreading function).

As to the means of calculating ξ, one might consider deriving a differential equation for ξ, as was done for ζ. That will not be necessary, however; ξ can be calculated from ζ:

$$\xi = \left.\frac{\partial r}{\partial \theta_s}\right|_{z=\text{const}} = -\left(\left.\frac{\partial r}{\partial z}\right|_{\theta_s=\text{const}}\right)\left(\left.\frac{\partial z}{\partial \theta_s}\right|_{r=\text{const}}\right) = -\frac{1}{z'}\zeta \quad . \tag{V.1}$$

Moreover, it is preferable from a computational standpoint to calculate ξ from ζ rather than attempt to solve a differential equation for ξ because ξ is singular at ray turning points (where $z'=0$), as inspection of Eq. V.1 will quickly disclose. These singularities would disrupt numerical solution of the differential equation. Thus, ζ serves not only in the calculation of intensity but also in the location of eigenrays.

It turns out that ξ' will also be needed. Differentiation of Eq. V.1 with respect to range holding θ_s constant yields

$$\xi' = -(\zeta'+z''\xi)/z' \quad . \tag{V.2}$$

1. Hermite Cubic Splines

The hermite cubic spline and the T-spline have quite different applications even though both fit data piecewise with cubic polynomials. Because both types of splines are used extensively and are easily confused, the uses of the splines will be distinguished here and the hermite cubic spline will be described.

T-splines are useful when the only available information about a function consists of sample values. In many cases, the sample values are obtained by measurements of a physical system and are expected

to be representative of a function which is in some sense smooth. The T-spline guarantees two continuous derivatives of the fitting function and is used to fit the sound speed profiles and bathymetry.

On the other hand, hermite cubic spline interpolation is used to approximate a known function when function evaluations are costly. It is more accurate than linear interpolation because use is made of the derivative of the function as well as the function itself. These splines are used to fit the $r(\theta_s)$ curves, for example.

Given a function $f(x)$, its derivative $f'(x)$, and the values $f(x_0)$, $f'(x_0)$, $f(x_1)$, $f'(x_1)$, the hermite cubic interpolating polynomial $f_c(x)$ applicable for $x_0 \leq x \leq x_1$ is

$$
\begin{aligned}
f_c(x) &= a_0 + a_1(x-x_0) + a_2(x-x_0)^2 + a_3(x-x_0)^3, \\
a_0 &= f(x_0), \\
a_1 &= f'(x_0), \\
a_2 &= 3[f(x_1 - f(x_0)]/\Delta x^2 - [2f'(x_0)+f'(x_1)]/\Delta x, \\
a_3 &= 2[f(x_0 - f(x_1)]/\Delta x^3 + [f'(x_0)+f'(x_1)]/\Delta x^2, \text{ and} \\
\Delta x &= x_1 - x_0.
\end{aligned}
$$

The interpolation error is

$$
f(x) - f_c(x) = \frac{(x-x_0)^2 (x-x_1)^2}{24} f^{(4)}(\nu) \qquad (V.3)
$$

for some ν in $[x_0,x_1]$. This error is proportional to Δx^4 provided $f(x)$ has four continuous derivatives in $[x_0,x_1]$. By contrast, the linear interpolation error is proportional to Δx^2.

Derivatives and integrals of $f_c(x)$ can also be used to estimate derivatives and integrals of $f(x)$. When $f_c(x)$ is differentiated, the interpolation error, $f'(x)-f_c'(x)$, is proportional to Δx^3; differentiation is therefore less accurate than interpolation. Integration of $f_c(x)$ over the interval $[x_0,x_1]$ yields the Euler-Maclaurin integration formula described in Section III.B.

2. Contents of the Ray History Records

Each ray history record is a record of the significant events which occurred during propagation of the ray in the order they occurred, plus quantitative data about each event. The quantitative information varies with the nature of the event. In this section, the events recorded are described, and the ancillary data stored with the events is specified. The reasons for including specific data items will become apparent when eigenray location and interpolation procedures are discussed later in this chapter. In general, just enough information is recorded to specify the location of the event and the ray path slope there, to carry out several kinds of interpolations, and to provide ray path information which experience has shown to be particularly useful. More specifically, the ray history records contain enough information about each ray in the sweep-out to (1) determine whether two rays bracket an eigenray of a receiver at a given range, (2) numerically determine eigenray launch angles, (3) accurately estimate eigenray arrival angles, path lengths, travel times, intensities, and phases and, for eigenrays which undergo bottom reflections, to determine the bottom intercepts, ray path slopes, and bottom slopes at each reflection point, and (4) permit accurate reconstruction of the ray path trajectories.

a. Surface Reflection

Whenever a ray reflects from the surface, the values of r and z' are recorded, along with z, which is of course zero.

b. Bottom Reflection

Upon bottom reflection, the values of r, z, z', z", ζ, ζ', and z'_B are stored. These quantities are used in eigenray interpolations to determine the point of bottom incidence (range and depth), the eigenray path slope at incidence, and the bottom slope at incidence.

c. Ray Splitting Point

As shown in Fig. 6 and discussed in Section V.A.3, rays launched at certain launch angles may encounter features in the sound speed profile which cause ray paths to diverge sharply in response to a slight change in launch angle, giving rise to discontinuities in the $r(\theta_s)$ diagram. The passage of a ray through a point of divergence is detectable. If, in advancing the ray path solution from r_1 to r_2, the ray path has an inflection point, that is, z" undergoes a sign change, but if $sign(z_1-z_2) \neq sign(z''_1)$, then the event, its location, and the path slope there are recorded. The location of the event coincides with the inflection point, which is found by assuming that z" varies linearly from r_1 to r_2 and finding the zero of z".

d. Receiver Depth Crossing

Whenever a ray crosses a specific receiver depth, the values of r, z, z', z", ξ, ξ', s, $\partial s/\partial\theta_s$, t, and $\partial t/\partial\theta_s$ are recorded at the point where the ray crosses the receiver depth. Also recorded are the number of surface reflections, bottom reflections, caustics, turning points, and ray splitting points (see Section V.A.2.d).

e. Turning Points

Turning points, where z'=0, are located by monitoring the ray trace for changes in the sign of z'. When one is detected, the

approximate range of the turning point is determined by fitting a hermite spline to z' and z" over the interval defined by the last step of the ray trace and finding the zero of the spline. The depth of the turning point is then obtained by fitting a hermite cubic spline to z and z' and evaluating the spline at the turning point range. The point and path slope are recorded.

f. Caustics

Caustics, points where $\zeta=0$, are located by monitoring the ray trace for changes in the sign of ζ. When one occurs, the range of the caustic is located approximately by fitting a hermite spline to ζ and ζ' over the last range step and determining the zero of the spline. The depth of the caustic is obtained by fitting a hermite cubic spline to z and z' over the range step and evaluating the cubic for z at the range of the caustic. The point and path slope are recorded.

g. Marker Points

One of the most useful functions of a ray model is to produce plots of the ray paths. The ray history records, containing as they do the locations of important events along the ray paths, furnish the information needed to generate ray plots and much else besides. A ray path is plotted by connecting the events in its ray history record with a smooth curve and drawing the curve.

To take full advantage of a ray history record to plot a ray trajectory, one extracts from the record the locations of the events *in order*, as well as the ray path slopes at the events. Hermite splines are used to connect each pair of events in turn, thus reconstructing the ray path in the intervals between the events. The smooth curve formed of the union of the splines is plotted to complete the drawing of the ray path.

However, there is no assurance that significant events will occur often enough to permit accurate reconstruction of the ray path. It is therefore necessary to insert periodically into the ray history record points whose only purpose is to mark more precisely the ray trajectory.

In order to know when, during the stepwise solution of the ray path equation, to introduce marker points into the history record, we need some means of determining when the solution has advanced so far beyond the last recorded event that later reconstruction of the ray path is compromised. Since the ray path is to be represented later by hermite cubic splines, we need to know when the spline will deviate unacceptably from the actual ray path.

Inspection of the hermite interpolation error (Eq. V.3) suggests that the largest error is to be expected near the midpoint of the interval of interpolation since the interpolation error at the interval endpoints is zero and since $z^{iv}(r)$ tends to vary slowly with range. But it is inconvenient and costly to compute a new spline after each step and evaluate the midpoint error.

A much more satisfactory means of estimating the midpoint error is, ironically, to compute the difference between the third order (cubic) hermite spline and the much more complex fifth order hermite spline at the midpoint. The fifth order spline would use not only r, z, and z', but also z" at the endpoints of an interval. The extra information makes the fifth order interpolation formula much more accurate than the third order formula, so that the difference between the third and fifth order formulas is a good estimate of the error in the third order formula.

But, if it is too costly and inconvenient to construct the third order spline after every step, then it is certainly out of the question to construct both a third order spline and a fifth

order spline after every step in order to difference them. However, the difference between the third and fifth order formulas, when evaluated at the midpoint, is a surprisingly simple expression:

$$z_3(r_0 + \frac{\Delta r}{2}) - z_5(r + \frac{\Delta r}{2}) = \frac{\Delta r}{64}\left\{2\left[z'(r_1)-z'(r_0)\right] - \Delta r\left[z''(r_0)+z''(r_1)\right]\right\} , \quad (V.4)$$

where r_0 is the range of the last point entered in the history record, r_1 is the range just attained with the last step of the ray trace, $\Delta r=r_1-r_0$, and z_3 and z_5 are the third and fifth order interpolation formulas. It is not necessary to construct splines in order to make use of Eq. V.4. After each step in the ray trace, the right-hand side of Eq. V.4 is evaluated and, if the resulting error estimate exceeds a tolerance, the point (r_1,z_1) is entered in the history record along with z_1'.

h. Ray Termination

Ray traces are ended under several user controlled conditions. Traces are terminated if a ray (1) reaches a maximum specified range, (2) exceeds a specified number of surface or bottom reflections, (3) is steeper than a given maximum ray path angle, or (4) strikes the bottom with a grazing angle exceeding a specified maximum. The ray termination point and the path slope are recorded.

3. Determination of the Eigenray Launch Angle

The simple $r(\theta_s)$ diagram of Fig. 6 contains many of the features of the more complex diagrams commonly encountered in practice. Three of these, described below, are critical to the location of eigenrays by interpolation.

(1) Rays launched at angles in the interval $(-2.0^o, 2.0^o)$ never reach the receiver depth; consequently, no ray

with a launch angle in this interval can be an eigenray.

(2) Rays launched at angles near -5^{o} and 5^{o} encounter a local maximum in the sound speed profile and diverge strongly. A discontinuity in $r(\vartheta_s)$ is created.

(3) Rays launched at $\pm 10^{o}$ graze the surface; rays launched at $\pm 15^{o}$ graze the bottom. At these angles, $\partial r/\partial \theta_s$ is discontinuous.

Although these features have been described specifically for the diagram of Fig. 6, in general there are ranges of values of θ_s for which $r(\theta_s)$ is not defined, and there will be values of θ_s for which $r(\theta_s)$ or $\partial r/\partial \theta_s$ is discontinuous.

In a range variable environment these features of $r(\theta_s)$ cannot be so readily identified with specific launch angles, yet it is not meaningful to attempt eigenray interpolations in a launch angle interval containing any of these features. Two rays are considered to bracket an eigenray if, and only if, (1) they differ by the launch angle increment $\Delta\theta_s$, (2) they bracket the receiver in range when they cross the receiver depth, and (3) the events in their ray history records occur in exactly the same sequence, with the following exception. If the history record of one ray shows that the ray passed through a caustic and then a turning point, while the companion ray passed through the turning point and then the caustic, it is nevertheless permissible to use these two rays for eigenray interpolation provided their history records are otherwise identical. This exception is allowed because no discontinuities in $r(\theta_s)$ or $\xi(\theta_s)$ arise from it.

When two rays satisfy these requirements, a hermite spline $r_c(\theta_s)$ is computed using the values of r_1, $(\partial r/\partial \theta_s)_1$, r_2, and $(\partial r/\partial \theta_s)_2$, where the subscripts denote evaluation at points 1 and 2 where the rays

cross the receiver depth. The eigenray launch angle is then determined by locating the zero of $r_c(\theta_s)-r_R$ numerically.

Successive approximations to the zero usually converge very nearly to the limits of precision of the computer within three iterations if Newton's method[28] is used. In general, if one is seeking a zero of the function $f(x)$ and x_0 is known to be a good approximation to the desired zero, then often an improved estimate, x_1, is given by Newton's iterative formula

$$x_1 = x_0 - f(x_0)/f'(x_0) \quad . \qquad (V.5)$$

To apply Eq. V.5 to the eigenray problem, one must be able to compute $r_c(\theta_s)-r_R$ and its derivative $dr_c/d\theta_s$. But $r_c(\theta_s)$ is simply a cubic polynomial and $dr_c/d\theta_s$ is the quadratic polynomial obtained by differentiating $r_c(\theta_s)$. Both functions can be evaluated very rapidly on a computer. Thus, hermite splines and Newton's method are well suited to each other and to the task of eigenray location. However, it should be emphasized that the true eigenray launch angle error depends less on the error in the zero of the cubic than the interpolation error committed by replacing $r(\theta_s)$ with $r_c(\theta_s)$. In order to keep the interpolation error small the ray sweep-out angle increment $\Delta\theta_s$ must be kept small.

B. Eigenray Path Data Interpolation

Having determined an eigenray launch angle, interpolations between the rays bracketing the eigenray yield additional information about the eigenray. In particular, interpolation gives the arrival angle, travel time, path length, and intensity of the eigenray when it arrives at the receiver. For eigenrays which undergo bottom reflections, the reflection points, the ray path angles at intercept, and the bottom

slope at intercept are also found. The interpolation methods are described below.

1. Arrival Information

In the formulas and derivations which follow, two rays bracketing the eigenray cross the receiver depth at points 1 and 2, where $\theta_{s1} < \theta_{s2}$. The eigenray launch angle is θ_{se}.

a. Arrival Angle

A hermite spline $z'_c(\theta_s)$ is defined on the interval $[\theta_{s1},\theta_{s2}]$ using the values z'_1, $(\partial z'/\partial\theta_s)_1$, z'_2, and $(\partial z'/\partial\theta_s)_2$. The arrival angle is

$$\theta_R = \tan^{-1}(z'_c(\theta_{se})) \quad . \tag{V.6}$$

The values of $\partial z'/\partial\theta_s$ are not available directly from the ray history records. They are computed using ξ' as follows:

$$\frac{\partial z'}{\partial\theta_s} = -z'\xi' \quad . \tag{V.7}$$

Note that here $\partial z'/\partial\theta_s$ is computed holding depth constant ($z=z_R$), whereas ζ' is computed holding range constant (see Section II.B); $\partial z'/\partial\theta_s$ as computed above is not to be confused with ζ'.

The above expression for $\partial z'/\partial\theta_s$ can be obtained by resorting to Taylor series expansions. In Fig. 8, two rays differing in

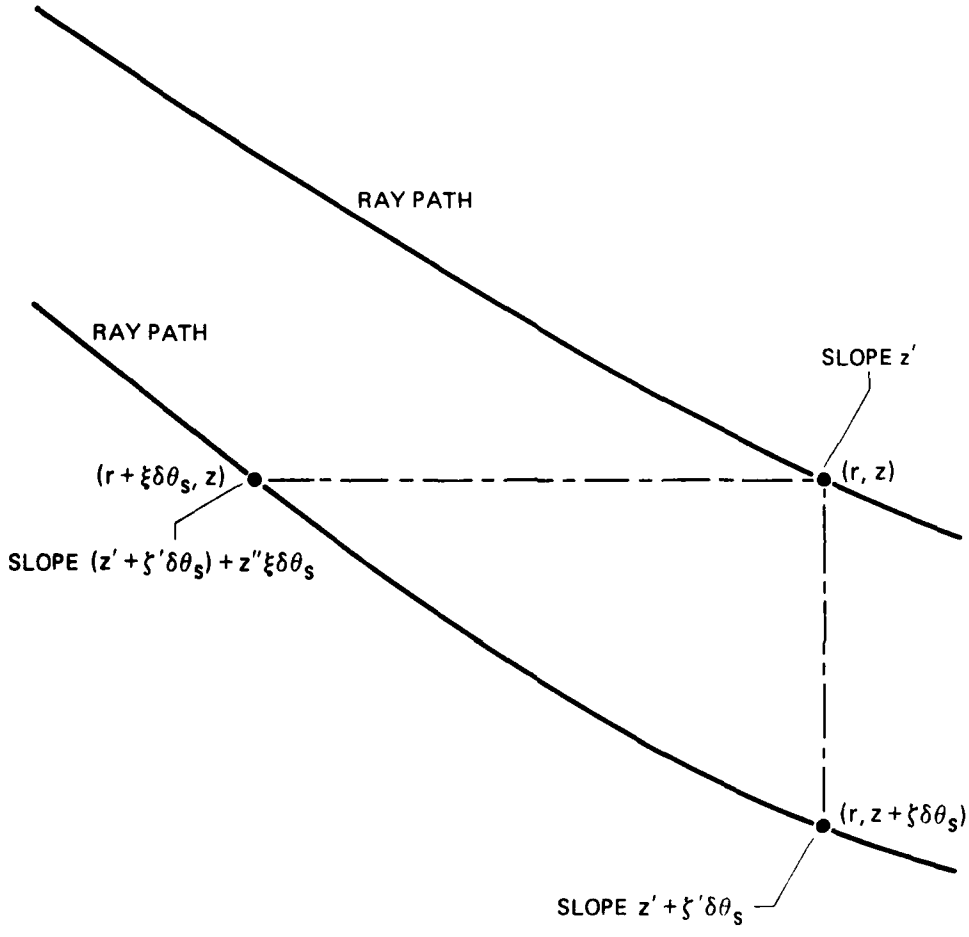

FIGURE 8
CONSTRUCTION OF $\partial z'/\partial\theta_s|z = z_R$

ARL:UT
AS-82-1670
TLF-GA
10-19-82

launch angle by $\delta\theta_s$ (not the sweep-out angle increment $\Delta\theta_s$) are shown as they pass near an observation point (r,z). The ray path slope at (r,z) is z'; at $(r,z+\zeta\delta\theta_s)$ the slope is $z'+\zeta'\delta\theta_s$ to first order. The slope at $(r+\xi\delta\theta_s,z)$ is therefore $(z'+\zeta'\delta\theta_s)+z''\delta\theta_s$, again to first order. Passing to the limit $\delta\theta_s \to 0$,

$$\left.\frac{\partial z'}{\partial \theta_s}\right|_{z=z_R} = \lim_{\delta\theta_s \to 0} \frac{\delta z'}{\delta \theta_s}$$

$$= \lim_{\delta\theta_s \to 0} \frac{(z'+\zeta\delta\theta_s) + z''\xi\delta\theta_s - z'}{\delta\theta_s}$$

$$= \zeta' + z''\xi$$

$$= -z'\xi' \quad , \qquad (V.8)$$

where use has been made of Eq. V.2.

b. Path Length

A hermite spline s_c is defined using the values s_1, $(\partial s/\partial\theta_s)_1$, s_2, and $(\partial s/\partial\theta_s)_2$. The path length is

$$s = s_c(\theta_{se}) \quad , \qquad (V.9)$$

where

$$\frac{\partial s}{\partial \theta_s} = \left(\left.\frac{\partial s}{\partial r}\right|_{\theta_s=\text{const}}\right)\left(\left.\frac{\partial r}{\partial \theta_s}\right|_{z=\text{const}}\right)$$

$$= \xi/\cos\theta \quad . \tag{V.10}$$

c. Travel Time

A hermite spline t_c is defined using the values t_1, $(\partial t/\partial\theta_s)_1$, t_2, and $(\partial t/\partial\theta_s)_2$. The travel time is

$$t = t_c(\theta_{se}) \quad , \tag{V.11}$$

where

$$\frac{\partial t}{\partial \theta_s} = \frac{n}{c_0}\frac{\partial s}{\partial \theta_s} \quad . \tag{V.12}$$

d. Intensity

A hermite spline r_c was defined using r_1-r_R, ξ_1, r_2-r_R, and ξ_2 in order to determine the eigenray launch angle:

$$r_c(\theta_s) = r_{c0} + (\theta_s-\theta_1)r_{c1} + (\theta_s-\theta_1)^2 r_{c2} + (\theta_s-\theta_1)^3 r_{c3} \quad , \tag{V.13}$$

where r_{c0}, r_{c1}, r_{c2}, and r_{c3} are the hermite spline coefficients. The derivative $dr_c/d\theta_s$, evaluated at θ_{se}, is

$$\xi_c(\theta_s) = r_{c1} + 2(\theta_{se}-\theta_1)r_{c2} + 3(\theta_{se}-\theta_1)^2 r_{c3} \quad . \quad \text{(V.14)}$$

Then, by Eq. II.29,

$$\frac{I}{I_0} = \left| \frac{\cos\theta_{se}}{r_R \xi_c(\theta_{se}) \sin\theta_R} \right| \quad . \quad \text{(V.15)}$$

2. Bottom Intercept Interpolation

In the following formulas and derivations, variables with subscripts 1 and 2 are evaluated at the points where rays intersect the bottom.

a. Eigenray Bottom Intercepts

The range at which the eigenray strikes the bottom is

$$r_B = r_{Bc}(\theta_{se}) \quad , \quad \text{(V.16)}$$

where r_{Bc} is the hermite spline defined by r_{B1}, $(\partial r_B/\partial\theta_s)_1$, r_{B2}, and $(\partial r_B/\partial\theta_s)_2$. Likewise, the depth at intercept is

$$z_B = z_{Bc}(\theta_{se}) \quad , \tag{V.17}$$

where z_{Bc} is defined by z_{B1}, $(\partial z_B/\partial\theta_s)_1$, z_{B2}, and $(\partial z_B/\partial\theta_s)_2$.

An expression for $\partial r_B/\partial\theta_s$ was developed in Section II.B:

$$\frac{\partial r_B}{\partial\theta_s} = \zeta \frac{1}{z'_B - z'_I} \quad .$$

From this expression, we can derive an expression for $\partial z_B/\partial\theta_s$.

$$\frac{\partial z_B}{\partial\theta_s} = \frac{\partial z_B}{\partial r_B}\frac{\partial r_B}{\partial\theta_s}$$

$$= \zeta \frac{z'_B}{z'_B - z'_I} \quad . \tag{V.18}$$

b. Ray Path Angle at Intercept

A hermite spline, z'_{Ic}, is defined by z'_{I1}, $(\partial z'_I/\partial\theta_s)_1$, z'_{I2}, and $(\partial z'_I/\partial\theta_s)_2$, where $\partial z'_I/\partial\theta_s$ is the rate of change of ray path slope at the bottom intercept with respect to launch angle. The path slope at intercept is

$$z'_I = \tan^{-1}\left(z'_{Ic}(\theta_{se})\right) \quad . \tag{V.19}$$

To find $\partial z_I'/\partial\theta_s$ by a Taylor series expansion we refer back to Fig. 3 in Chapter II, where we see that

$$\frac{\partial z_I'}{\partial\theta_s} = \lim_{\delta\theta_s \to 0} \frac{z_2' - z_1'}{\delta\theta_s} \quad . \tag{V.20}$$

An expression for z_2', Eq. II.48, was developed in Section II.B:

$$z_2' = z_1' + \delta\theta_s\left(\frac{\partial r_B}{\partial\theta_s} z_1'' + \zeta_1'\right) + \ldots \quad ,$$

so that

$$\frac{\partial z_I'}{\partial\theta_s} = \zeta_I \frac{z_I''}{z_B' - z_I'} + \zeta_I' \quad . \tag{V.21}$$

c. Bottom Slope at Intercept

A hermite spline, z_{Bc}', is defined using z_{B1}', $(\partial z_B'/\partial\theta_s)_1$, z_{B2}', and $(\partial z_B'/\partial\theta_s)_2$. The bottom slope at intercept is

$$z_B' = \tan^{-1}\left(z_{B_c}'(\theta_{se})\right) \quad . \tag{V.22}$$

To find $\partial z'_B/\partial\theta_s$ we again refer to Fig. 3 in Chapter II and find that

$$\frac{\partial z'_B}{\partial \theta_s} = \lim_{\delta\theta_s \to 0} \frac{z'_{B2} - z'_{B1}}{\delta\theta_s} \quad . \tag{V.23}$$

Equation II.49 is an expression for z'_{B2}:

$$z'_{B2} = z'_{B1} + \delta\theta_s \frac{\partial r_B}{\partial \theta_s} z''_{B1} + \cdots \quad .$$

Combining Eqs. V.23 and II.49 yields

$$\frac{\partial z'_B}{\partial \theta_s} = \zeta_I \frac{z''_B}{z'_B - z'_I} \quad . \tag{V.24}$$

C. Summary

In this chapter, the procedure used to locate eigenrays by interpolation between rays traced during a sweep-out was described. Also presented were the interpolation methods used to determine eigenray arrival data and eigenray bottom reflection information.

VI. ORGANIZATION OF MEDUSA

The ray model described in Chapters II through V of this report is implemented on a CDC CYBER 171 as a package of FORTRAN programs, collectively referred to as MEDUSA. Figure 9 is a schematic diagram of MEDUSA, showing the programs in the package, the data required by the programs, and the output produced by them.

The organization of MEDUSA is unusual in that the various functions of the model are performed by separate programs. Each program performs a very limited computational or display task. In some cases, the output from one program is used as input by several other programs. In the more common configuration, a model is implemented as a single large program, and all of the functions and capabilities of the model are incorporated in the program. The compartmentalized design of MEDUSA, however, has several advantages. It makes the system more compact and reliable. Modifications and additions are more easily implemented than they would be in a monolithic program, and the many pathways through the system make it possible to recombine and display ray information in a variety of ways.

The components of the package can be roughly categorized as environmental preprocessing and display routines, ray tracing programs, and eigenray, propagation loss, and diagnostic postprocessors. Their functions and relations to each other are briefly summarized here. Their use is illustrated in the next chapter.

In the first category is ENVPLT. ENVPLT plots the sound velocity profiles and bathymetry. It is used for graphical display of the environment, which is usually received in the form of tabulated data. Such displays are informative in their own right, and they may reveal input data errors.

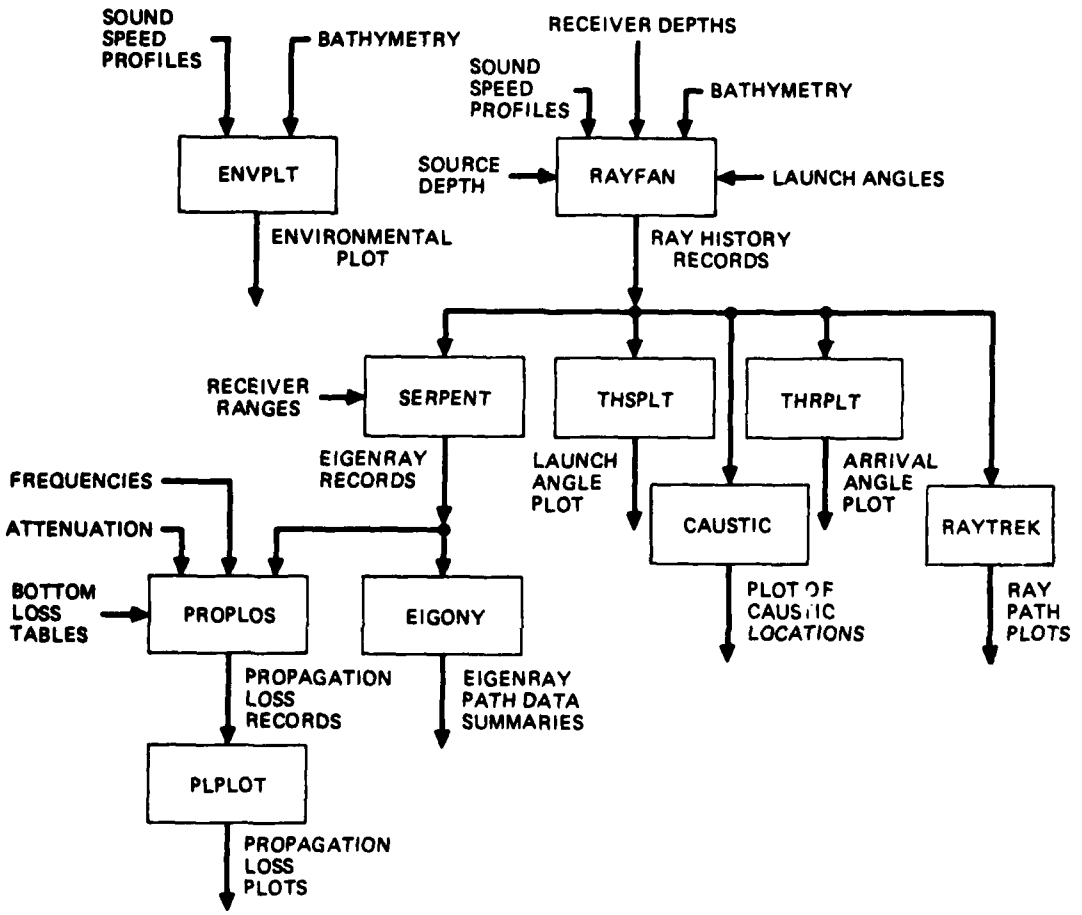

FIGURE 9
ORGANIZATION OF MEDUSA

ARL:UT
AS-83-1191
TLF - GA
11-8-83

Also in the first category are programs which format data from environmental databases for use by MEDUSA. The author has assisted in the installation of MEDUSA at computer facilities which possess databases containing archives of sound velocity profiles, bathymetry, and bottom loss data. At each computer site, programs convert the archival data retrieved by the database system into the format required by MEDUSA.

RAYFAN is the program responsible for tracing rays and generating ray history records, which are very lengthy and so are stored on a disk. In addition to the environmental data, RAYFAN requires as input the source depth, the launch angles to be used in the sweep-out, and the depths of all receivers for which eigenrays will be required. The ray history records produced are used by a growing array of postprocessors.

RAYTREK plots the ray paths of any of the rays recorded in the ray history records.

CAUSTIC plots the locations of caustics encountered during the ray sweep-out.

THSPLT produces plots of $r(\theta_s)$; THRPLT plots arrival angles as a function of receiver range.

SERPENT locates eigenrays by interpolation of the ray histories and generates eigenray path history records. The eigenray records are also extremely lengthy and therefore are stored on a disk also. EIGONY prints eigenray path summaries for specified receivers.

PROPLOS adds the pressure contributions of the eigenrays and computes propagation loss. PLPLOT plots the propagation loss curves.

VII. APPLICATIONS

This chapter illustrates the use of the MEDUSA programs. For the example presented here, the environment, particularly the bathymetry, changes rapidly with range, bottom interaction effects are important, and the track ranges are relatively short. MEDUSA has also been used in long range propagation analysis problems. The computer resources required have proved to be remarkably insensitive to the ranges involved. For the long range case, long ray traces are compensated by the reduced number of rays to be traced and the small path angles involved.

Each use of MEDUSA begins with the generation of environmental plots by ENVPLT. Figure 10 is the graphical output from ENVPLT for this example. The bathymetry and sound speed profiles are presented to the programs as tabulated data in the usual fashion. The tabulated sound speed and bathymetry points supplied to ENVPLT are plotted as discrete points. The smooth curves interpolating the user supplied data points are generated by repeated evaluation of the bathymetric and sound speed profile T-splines at finely spaced intervals of depth and range. Several sound speed profiles are also shown in Fig. 10 between the user supplied profiles. These profiles, distinguished by the absence of accompanying discrete data points, are intermediate profiles which show how the profiles evolve with range from one user supplied profile to the next. Environmental plots thus provide not only a graphical representation of the somewhat cryptic tabulated data, but are also a valuable diagnostic aid against input data errors, undersampling of the environment, and possible range interpolation anomalies in the sound speed profiles.

Occasionally, usually for special research purposes, a user will supply sound speeds or bathymetry to MEDUSA as mathematical functions of his own devising, bypassing the standard procedure of fitting T-splines to tabulated data. ENVPLT will then produce plots of the user defined environmental functions. The substitutions pose no

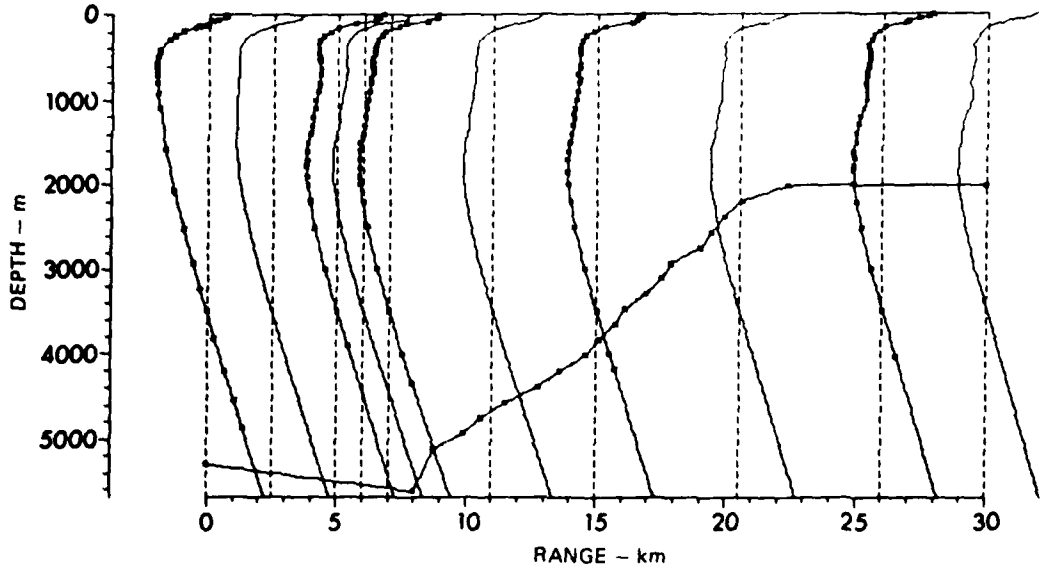

FIGURE 10
SOUND SPEED PROFILES AND BATHYMETRY (ENVPLT)

ARL:UT
AS-83-1192
TLF · GA
11 · 8 · 83

special problems for MEDUSA, provided the functions possess the required degrees of continuity discussed in Chapters III and IV.

Once satisfied with MEDUSA's representation of the environment, the next step is usually to produce ray path plots, such as Fig. 11. In this example, the source is located 1 m above the bottom at a depth of 5303 m. This is accomplished by tracing a few rays with RAYFAN and plotting the ray paths using RAYTREK. These plots are often all that is required of MEDUSA, but they can also convey very quickly to an experienced user a great deal of information about the effects of bathymetry and range and depth variations of the sound speed on sound propagation. Thus, RAYTREK is often used as a survey tool in preparation for eigenray and propagation loss calculations.

In order to proceed beyond the generation of ray path plots, a ray sweep-out is performed with RAYFAN, in which hundreds of rays are traced in fine increments of the launch angle to a maximum range beyond the range of the most distant receiver of interest. The ray history records generated form the basis for all further processing. In this example, the rays traced had launch angles ranging from -50^{o} to 50^{o} in 0.5^{o} increments, except for the interval from -10^{o} to 10^{o}, where a finer 0.25^{o} increment was used. A receiver depth of 18.3 m (60 ft) was specified. Rays were traced to a maximum range of 35 km.

Figure 12, generated by program CAUSTIC, shows the caustics encountered by the rays during the sweep-out. Unusually high signal pressure levels occur near caustics, which are focal points of acoustic energy. Although the ray theory approximation $K \neq k$ is invalid within a few wavelengths of a caustic, the effect of the approximation is always to cause uncorrected ray theory to overestimate the pressure near a caustic. Thus, ray theory predictions of the locations of acoustic focal points are accurate, although predictions of actual signal pressure are exaggerated extremely close to them. Corrections can be made to revise ray theory pressure predictions downward and such corrections are likely

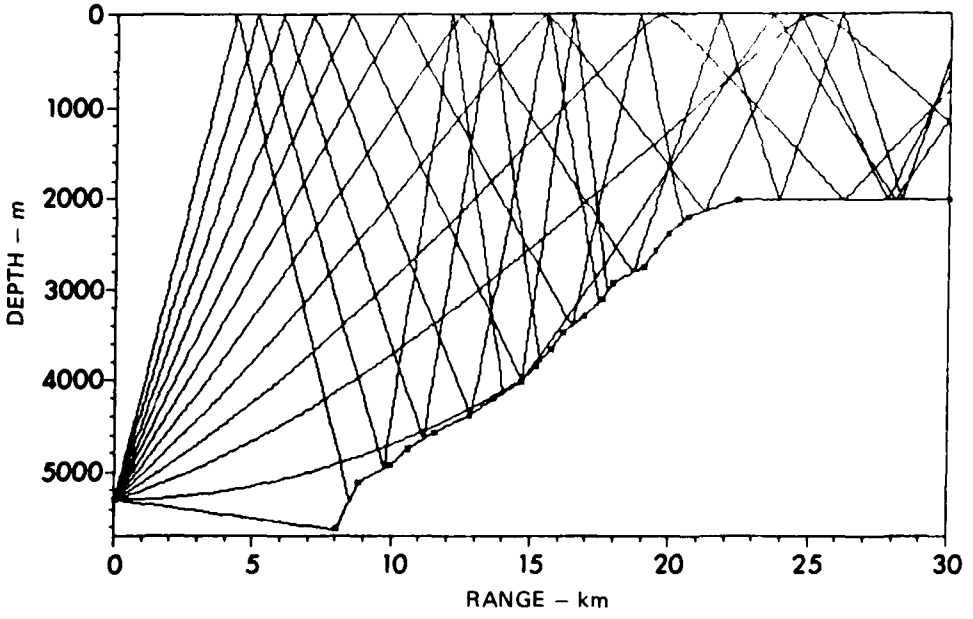

FIGURE 11
RAY PATH PLOT (RAYTREK)

ARL:UT
AS-83-1193
TLF - GA
11-8 83

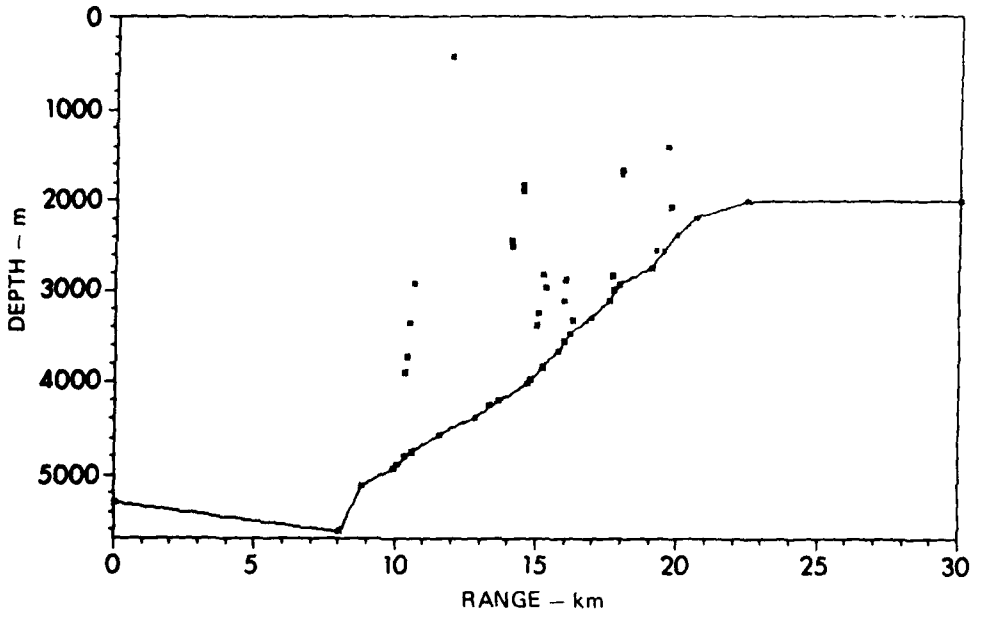

FIGURE 12
CAUSTICS (CAUSTIC)

ARL:UT
AS-83-1194
TLF-GA
11-8-83

to be introduced into MEDUSA at a later time. In any case, Fig. 12 shows the caustics are well below the 18.3 m receiver depth and we need not be concerned with them in this example.

THSPLT produced the $r(\theta_s)$ plot of Fig. 13. Each point on the plot represents a range at which a ray crossed the receiver depth and the launch angle of the ray. The fine sampling of launch angles causes the points to pack closely together, so that they tend to form smooth curves, although the curves do have discontinuities and cusps. The intersections with the curves of a straight line, drawn across the plot at a constant range corresponding to a receiver range, occur at launch angles corresponding to eigenray launch angles. By moving the straight line back and forth over the plot to represent receivers at various ranges, one can observe the eigenray launch angles changing as the line intersects different parts of the curves.

The arrival angle diagram of Fig. 14 was produced by THRPLT in much the same way as THSPLT generated the launch angle diagram of Fig. 13; the points on the arrival angle diagram indicate the ranges where rays crossed the receiver depth and the angles the ray paths made with respect to the horizontal as they crossed the receiver depth. The intersections of the arrival angle curves with a straight line, drawn across the plot at a given receiver range, indicate the expected ray arrival angles for a receiver at that range. By varying the receiver range, one can tell at a glance which arrival angles to expect at various receiver ranges and how the arrival angle structure may be expected to change with range.

The preceding display programs, except ENVPLT, all simply plotted information stored in the ray history files. To proceed beyond this point, further processing is necessary. The next step is to locate eigenrays, using SERPENT to perform eigenray interpolations on the data stored in the ray history records. SERPENT will produce eigenray history records.

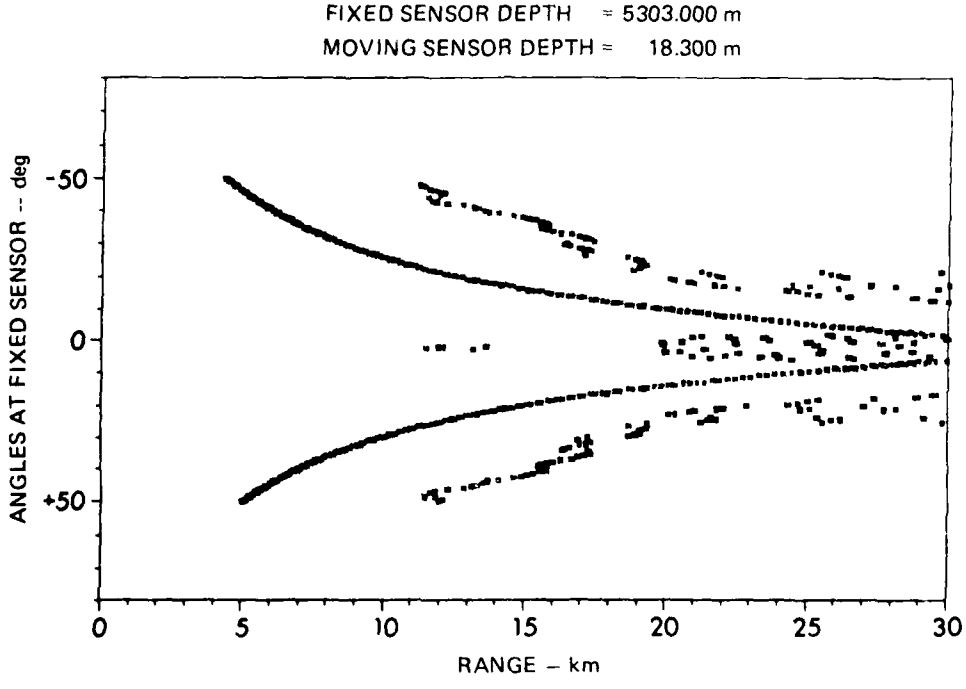

FIGURE 13
$r(\theta_s)$ FOR RANGE DEPENDENT MEDIUM (THSPLT)

ARL UT
AS-83-1195
TLF-GA
11-8-83

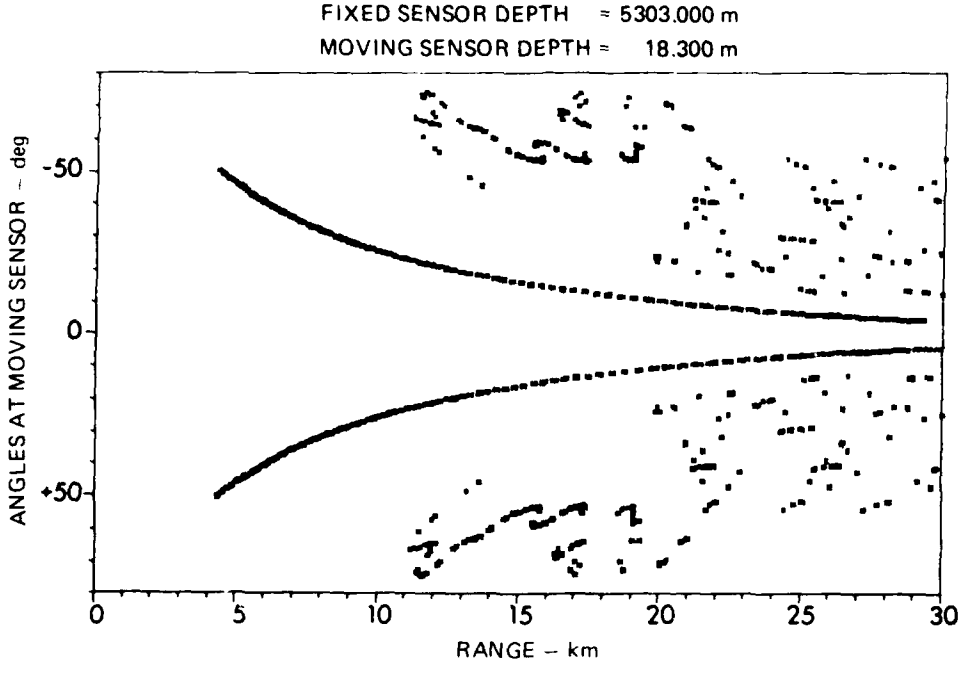

FIGURE 14
ARRIVAL ANGLES (THRPLT)

ARL:UT
AS-83-1196
TLF-GA
11-8-83

EIGONY will display any desired portion of the eigenray records. Figure 15 shows a very brief excerpt from the output normally generated by EIGONY. Here, we see that SERPENT found eight eigenrays for the receiver located at a range of 14 km and a depth of 18.3 m. For each of those eigenrays, EIGONY prints the launch and arrival angle, the travel time, the number of surface and bottom reflections the eigenray underwent and the number of caustics it passed through on the way to the receiver, and the acoustic pressure at the receiver. The pressure is computed according to the geometrical spreading law of Eq. II.29; the frequency dependent effects of volumetric attenuation in the water and bottom loss are accounted for later. For each bottom reflection which an eigenray undergoes, EIGONY prints the location of the bottom intercept, the bottom slope angle, and the grazing angle (the angle of the ray with respect to the bottom at the intercept).

PROPLOS adds the complex eigenray pressure contributions at each of the receiver locations. If the user specifies tables of reflection coefficients (which are generally frequency dependent), then the reflection loss and phase shift due to each bottom reflection of each eigenray are figured into the pressure summation. At the same time, if the user wishes to apply a frequency dependent volumetric attenuation coefficient, then those losses are taken into account also. The total complex pressure P at a given receiver is

$$P = \sum_{m=1}^{N} \left(10^{-\alpha s_m/20} A_m e^{j\omega t_m} e^{-j\pi n_s} e^{-j\frac{\pi}{2} n_c} \prod_{\ell=1}^{N_b} R_{m\ell} \right) \qquad \text{(VII.1)}$$

where N is the number of eigenrays, α is the attenuation (dB/m), s_m is the path length of the mth eigenray, t_m is the travel time of the mth eigenray, n_s is the number of surface reflections, n_c is the number of caustics, N_b is the number of bottom reflections, and $R_{m\ell}$ is the complex

SOURCE DEPTH (M) = 5303.000
RECEIVER DEPTH (M) = 18.300

RECEIVER RANGE (KM) = 14.000

SSS	SOURCE ANGLE (DEG)	ARRIVAL ANGLE (DEG)	PRESSURE	TIME (SEC)	NO. SUR RFL	NO. BOT RFL	NO. CST	BOTTOM REFLECTION DATA RANGE (KM)	DEPTH (M)	GRAZING ANGLE (DEG)	BOT ANGLE (DEG)
1	-38.940	-60.127	3.38E-05	13.484	1	1	0	11.459	4583.185	50.102	-10.229
2	-38.962	60.272	3.42E-05	13.504	2	1	0	11.452	4584.420	50.183	-10.292
3	-17.039	-17.442	8.02E-05	9.890	0	0	0				
4	-17.226	17.627	7.98E-05	9.897	1	0	0				
5	1.962	-43.067	1.23E-05	10.510	0	1	0	8.771	5147.862	19.464	-23.531
6	2.812	-42.884	1.04E-05	10.500	0	2	0	.120 8.770	5308.831 5147.586	.432 19.313	2.298 -23.393
7	21.645	-17.452	7.92E-05	9.890	0	1	0	.003	5304.112	19.365	2.298
8	21.833	17.631	7.88E-05	9.897	1	1	0	.003	5304.111	19.533	2.298

FIGURE 15
EIGENRAY PATH SUMMARIES (EIGONY)

ARL:UT
AS-83-1197
TLF-GA
11-8-83

reflection coefficient for the ℓth bottom reflection of the mth eigenray. The phase inversion of a ray upon surface reflection arises from the representation of the surface as a flat pressure release perfect reflector. Notice the $-\pi/2$ phase shift as a ray passes through a caustic.[8] The sign of the phase shift is often reversed (incorrectly) in ray models, and the phase shift itself is sometimes mistakenly associated with turning points rather than caustics.

The coherent propagation loss is

$$PL_{coh} = -10 \log_{10} PP^{*} \quad . \qquad \text{(VII.2)}$$

The incoherent propagation loss is defined to be

$$PL_{incoh} = -10 \log_{10} \left[\sum_{m=1}^{N} A_m^2 \left(\prod_{\ell=1}^{N_b} R_{m\ell} R_{m\ell}^{*} \right) \right] \quad . \qquad \text{(VII.3)}$$

Here, the root-mean-square pressures are added without regard to phase. This procedure is not well justified mathematically, but it does yield propagation loss curves (the "incoherent" propagation loss) which vary more slowly with range than the coherent propagation loss, and which, in some cases, seem to approximate a range averaged coherent propagation loss. In any event, the incoherent propagation loss is frequently required of a ray model and must be provided.

PROPLOS computes, prints, and stores on disk the coherent propagation loss, the incoherent propagation loss, and the incoherent propagation loss computed assuming an infinitely rigid, perfectly reflecting bottom.

PLPLOT plots the propagation loss computed by PROPLOS. Figure 16 shows the coherent and incoherent propagation loss curves for a frequency of 150 Hz and an attenuation of 1.5×10^{-6} dB/m. Bottom loss tables were also specified, so that each time an eigenray struck the bottom it incurred some grazing angle dependent loss but no phase shift. Figure 16 also shows the incoherent propagation loss for an infinitely rigid, perfectly reflecting bottom. The difference between the incoherent propagation loss curves for the reflecting bottom and the partially absorbing bottom gives a quick indication of the importance of the bottom in propagation analysis.

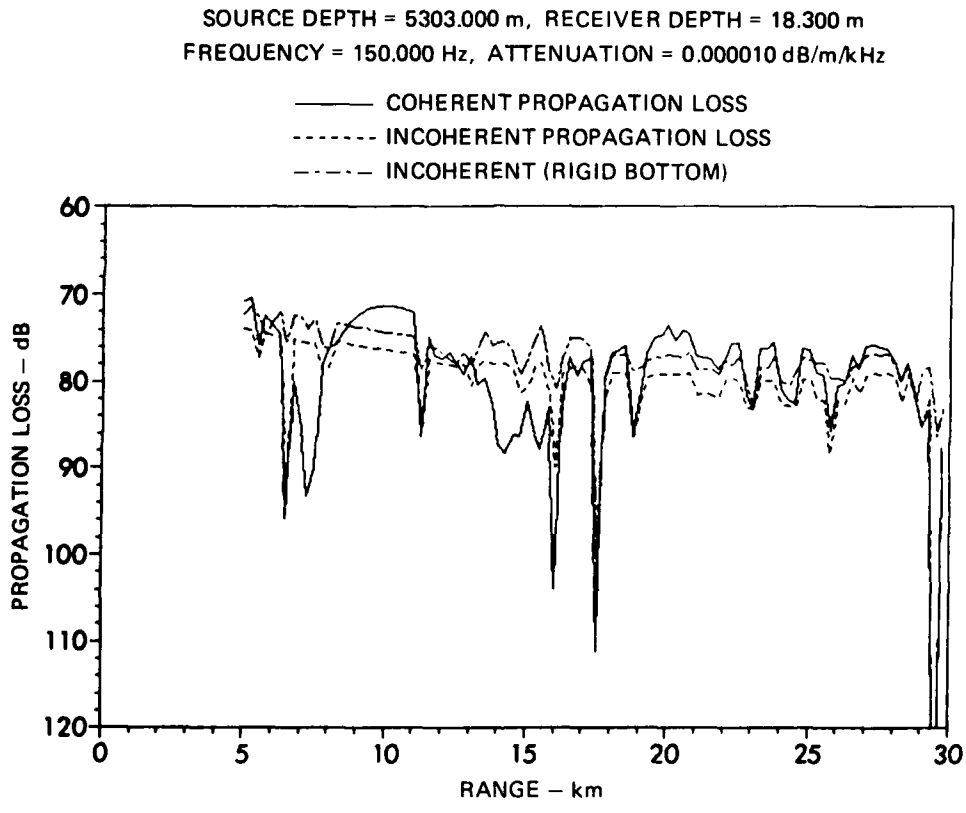

FIGURE 16
PROPAGATION LOSS (PLPLOT)

ARL:UT
AS-83-1198
TLF - GA
11-8-83

VIII. CONCLUSION

When ray models began to make the transition from range invariant to range dependent media, many of the techniques developed for range independent media were no longer applicable. In range independent environments, the ray paths are periodic functions of range, and a ray with a given launch angle has a characteristic period, or cycle distance. The first ray models fully exploited that fact to greatly simplify ray tracing and locating eigenrays (see Ref. 11).

Since rays in a horizontally stratified medium are cyclic, it is only necessary to perform the calculations needed to trace a ray through half of a cycle; the ray trajectory can then be extrapolated to any desired range by connecting half cycle paths and segments of half cycle paths. Thus, range independent ray models could trace rays very rapidly. Most such models used analytical solutions of the ray equations (see Section III.A), although this was not necessary and, in retrospect, probably set an unfortunate precedent.

It was possible and very useful in horizontally stratified media to be able to classify rays and eigenrays according to just four criteria: the sign of the ray launch angle (whether the ray was upgoing or downgoing at the source), the sign of the arrival angle (whether the ray was upgoing or downgoing at the receiver), the number of cycles, and whether the ray reflected from the surface or bottom or had turning points instead of relections. The launch angle intervals giving rise to the various ray categories could be readily determined from the sound speed profile, Snell's law, and the range. It was also possible to determine whether there were any eigenrays belonging to a particular classification for a receiver at a particular range. Thus, eigenrays could be located by systematic exploration of each of the ray categories.

It was even possible to locate an eigenray of known classification by numerical shooting methods (see Ref. 11).

But rays in range variable environments are not periodic functions, and Snell's law is no longer applicable. New strategies for tracing rays and locating eigenrays in these more challenging environments have been the subject of this report.

It is no longer sufficient in such media to perform ray trace calculations over a half cycle; rays must be traced out in full, at substantially greater computational cost. There are compelling reasons for seeking numerical, rather than analytical, solutions to the ray equations. With that in mind, the equations for the ray path trajectory and intensity are written in terms of differential equations in a form proposed by Solomon and Armijo,[18] because a great variety of methods exist for solving differential equations numerically. Chapter III discusses the numerical alternatives in terms of the particular problem at hand and arrives at a suitable method which, although somewhat slow, is very accurate, flexible, simple, and reliable. The method, Kutta's third order rule, lacks a procedure for estimating errors. An independent means of error estimation and control is therefore developed.

Some of the ray path information, namely the path length and travel time, can be conveniently expressed as ray path integrals and computed numerically. An appropriate numerical integration method, based on an Euler-Maclaurin formula, is explained.

When rays reflect from the surface or bottom, the solutions of the ray path and intensity differential equations must be restarted at the boundary intersection with new initial values. The reinitialization conditions for the ray path equation are easily derived from geometrical considerations since it is assumed that rays undergo specular reflection from boundaries. But the effects of reflections from boundaries on ray path spreading are more complicated. The reinitialization equations for

ray path spreading, derived in Section II.B, correctly account for the effects of ray path curvature, and for the curvature of the bottom when applicable.

The solution of the ray equations is very sensitive to the representation of the sound speed and bathymetry within the model, and the location of eigenrays depends critically on a condign treatment of the environment. Sound speeds and bathymetry are normally supplied to a ray model as tables of values measured at various ranges and depths. The ray model must fit the tabulated data with interpolating functions so that the sound speed and bottom depth can be determined away from the tabulated points. The interpolating functions should possess two continuous derivatives in order to avoid propagation loss anomalies and to ease the task of eigenray location. The functions and their derivatives should be easy to evaluate on a computer.

Cubic splines had been proposed as suitable interpolating functions, and had even been incorporated into some ray models. But when the author applied cubic splines to tabulated bathymetry, it was soon discovered that the splines would usually exhibit nonphysical contortions. Attempts to suppress the formation of these spline artifacts, by tediously inserting new points into the bathymetry tables, often ended in frustration when the spline would perversely introduce new artifacts elsewhere. Spline artifacts also appeared occasionally in sound speed profiles.

The problem of spline artifacts was eventually solved by abolishing the cubic splines which gave rise to them in favor of modified splines devised by the author, called T-splines. T-splines and the environment are discussed in Chapter IV.

One of the principal duties of a ray model is to locate eigenrays and determine the ray path histories of the eigenrays. With this capability, the user of a ray model can identify the paths along

which energy is delivered to the receiver. Eigenrays are located in a range dependent medium by interpolating between rays, traced during an extensive ray sweep-out, which bracket a receiver in some sense. The precise determination of when it is appropriate to make eigenray interpolations and how to obtain eigenray path information by interpolation are two of the major achievements discussed in this thesis (see Chapter VI). Ray history records of sequences of hundreds of judiciously selected events, such as bottom reflections and passage through caustics, contain information crucial to both enterprises. The concept of the ray history record derives, greatly elaborated, from the ray classification scheme of range independent models, which had only four elements. Eigenray path data interpolation methods make use of hermite cubic interpolatory splines to fit data stored in the history records, and are far more accurate than the first order finite difference methods commonly used.

Ray models traditionally have played an important role in underwater acoustics research, and it is anticipated that their role will expand as their capabilities increase and new applications are found for them. Some of the improvements and extensions likely to be undertaken soon are described below.

It is expected that efforts to develop significantly faster ray trace methods will be made in the near future. Success in this rather prosaic matter would nevertheless greatly encourage the distribution and usage of ray models.

Range dependent ray models are poised to receive a plethora of wave theory modifications and corrections which are designed to improve their treatment of caustics, ducts, shadow zones, and surface and bottom interactions. Some range invariant ray models already contain these improvements; it remains only to generalize them to range dependent media.

The MEDUSA model is, at present, restricted to cylindrically symmetrical environments but, with minor modifications, it will be extended to certain kinds of three-dimensional environments which possess some form of azimuthal or translational symmetry. The preliminary studies of propagation across idealized eddies, fronts, and seamounts, and of oblique propagation over ridges and continental slopes can be conducted without resort to fully three-dimensional models. For this reason, the development of general purpose three-dimensional models may be premature at present.

It is hoped that this report will serve to describe some of the practical matters which must be considered when implementing or simply using ray models (particularly the MEDUSA ray model), and to suggest areas of further research which would extend the capabilities and applications of ray models.

BIBLIOGRAPHY

1. Joseph B. Keller and John S. Papadakis (editors), Wave Propagation and Underwater Acoustics (Springer-Verlag, New York, 1977).

2. A. D. Pierce, "Extension of the Method of Normal Modes to Sound Propagation in an Almost-Stratified Medium," J. Acoust. Soc. Am. 37, 19-27 (1965).

3. H. Weinberg and R. Burridge, "Horizontal Ray Theory for Ocean Acoustics," J. Acoust. Soc. Am. 55, 63-79 (1974).

4. Richard Pitre, "On the Application of Horizontal Ray Theory to Acoustic Propagation in the Ocean Waveguide," Ph.D. Dissertation, Physics Department, The University of Texas at Austin, Austin, Texas, 1984.

5. F. D. Tappert, in Wave Propagation and Underwater Acoustics, op. cit., Chapter 5, pp. 224-281.

6. D. M. Milder, "Ray and Wave Invariants for SOFAR Channel Propagation," J. Acoust. Soc. Am. 46, 1259-1263 (1969).

7. S. R. Rutherford, "An Examination of Coupled Mode Theory as Applied to Underwater Sound Propagation," Ph.D. Dissertation, Engineering Department, The University of Texas at Austin, Austin, Texas, 1979.

8. D. Ludwig, "Uniform Asymptotic Expansions at a Caustic," Commun. Pure Appl. Math. 19, 215-250 (1966).

9. D. White and M. Pedersen, "Evaluation of Shadow-Zone Fields by Uniform Asymptotics and Complex Rays," J. Acoust. Soc. Am. 69, 1029-1059 (1981).

10. E. L. Murphy and J. A. Davis, "Modified Ray Theory for Bounded Media," J. Acoust. Soc. Am. 56, 1747-1760 (1974).

11. Terry L. Foreman, "Acoustic Ray Models Based on Eigenrays," Applied Research Laboratories Technical Report No. 77-1 (ARL-TR-77-1), Applied Research Laboratories, The University of Texas at Austin, April 1977.

12. B. G. Roberts, Jr., "Horizontal-Gradient Acoustical Ray-Trace Program TRIMAIN," NRL Report No. 7827, Naval Research Laboratory, Washington, DC, 1974.

13. John J. Cornyn, "GRASS: A Digital-Computer Ray-Tracing and Transmission-Loss-Prediction System," Vol. 1, NRL Report No. 7621, Naval Research Laboratory, Washington, DC (1973).

14. C. B. Officer, Introduction to the Theory of Sound Transmission, with Applica[illegible] to the Ocean" (McGraw-Hill Book Co., Inc., New York, 1958).

15. I. Tolstoy and C. S. Clay, Ocean Acoustics (McGraw-Hill Book Co., Inc., New York, 1966).

16. Leonid M. Brekhovskikh, Waves in Layered Media (Academic Press, New York, 1960).

17. David M. Young and Robert T. Gregory, A Survey of Numerical Mathematics (Addison-Wesley Publishing Co., Reading, Massachusetts, 1972), Vol. 1, pp. 2-7.

18. L. P. Solomon and L. Armijo, "An Intensity Differential Equation in Ray Acoustics," J. Acoust. Soc. Am. 50, 960-963 (1971).

19. M. A. Pederson, "Acoustic Intensity Anomalies Introduced by Constant Velocity Gradients," J. Acoust. Soc. Am. 33, 465-474 (1961).

20. Young and Gregory, op. cit., pp. 473-490.

21. Ibid.

22. Young and Gregory, op. cit., pp. 344-374.

23. Young and Gregory, op. cit., pp. 365-368.

24. E. Fehlberg, "Klassiche Runge-Kutta-Formeln vierter und niedrigerer Ordnung mit Schrittweiten-Kontrolle und ihre Anwendung auf Wärmeleitungsprobleme," Computing 6, 61-71 (1970).

25. Young and Gregory, op. cit., pp. 296-301.

26. C. B. Moler and L. P. Solomon, "Use of Splines and Numerical Integration in Geometrical Acoustics," J. Acoust. Soc. Am. 48, 739-744 (1970).

27. Young and Gregory, op. cit., pp. 288-295.

28. Young and Gregory, op. cit., pp. 132-135.

1 December 1983

DISTRIBUTION LIST FOR
ARL-TR-83-41
UNDER CONTRACT N00014-82-C-0049

Copy No.

Commanding Officer
Naval Ocean Research and Development Activity
NSTL Station, MS 39529
1 Attn: E. D. Chaika (Code 530)
2 R. Gardner (Code 501)
3 D. B. King (Code 321)
4 W. A. Kuperman (Code 320)
5 CDR M. McCallister (Code 522)
6 R. Martin (Code 110A)
7 J. Matthews (Code 362)
8 W. W. Worsley (Code 110A)

Chief of Naval Research
Department of the Navy
Arlington, VA 22217
9 Attn: M. McKisic (Code 4250A)
10 R. Obrochta (Code 425 AR)

Office of Naval Research Detachment
Naval Ocean Research and Development Activity
NSTL Station, MS 39529
11 Attn: G. Morris (Code 425GG)
12 LCDR M. MCDonald (Code 425GG)

Commanding Officer
Naval Electronic Systems Command
Department of the Navy
Washington, D.C. 20360
13 Attn: LCDR S. Hollis (Code 612)
14 R. Mitnick (Code 612)
15 CDR C. Spikes (PDE 124-60)
16 L. Parish (PDE 124-50)

Director
Naval Research Laboratory
Department of the Navy
Washington, D.C. 20375
17 Attn: B. B. Adams (Code 8160)

Distribution list for ARL-TR-83-41 under Contract N00014-82-C-0049 (cont'd)

Copy No.

Commanding Officer
Naval Ocean Systems Center
Department of the Navy
San Diego, CA 92152
18 Attn: E. L. Hamilton
19 M. A. Pederson
20 H. P. Bucker

Commander
Naval Sea System Command
Department of the Navy
Washington, D.C. 20362
21 Attn: C. D. Smith (Code 63R)
22 D. E. Porter (Code 63R1)

Chief of Naval Operations
Department of the Navy
Washington, D.C. 20350
23 Attn: CAPT E. Young (OP 952D)

Chief of Naval Material
Department of the Navy
Washington, D.C. 20360
24 Attn: CAPT J. Harlett (MAT 0724)

25 Commander
Naval Surface Weapons Center
White Oak Laboratory
Department of the Navy
Silver Spring, MD 20910

26 Commander
David W. Taylor Naval Ship Research and Development Center
Department of the Navy
Bethesda, MD 20034

Naval Oceanographic Office
Department of the Navy
NSTL Station, MS 39522
27 Attn: W. Jobst (Code 7300)
28 J. Allen (Code 7310)
29 R. Hecht (Code 7332)

Distribution list for ARL-TR-83-41 under Contract N00014-82-C-0049 (cont'd)

Copy No.

Commander
Naval Air Development Center
Department of the Navy
Warminister, PA 18974
30 Attn: C. L. Bartberger

Officer in Charge
New London Laboratory
Naval Underwater Systems Center
Department of the Navy
New London, CT 06320
31 Attn: B. Cole
32 F. R. DiNapoli
33 P. Herstein

34 Director Naval Warfare
Deputy Undersecretary Defense R&E
Room 3D1048, Pentagon
Washington, D.C. 20301

OASN (R,E&S)
Room 4D745, Pentagon
Washington, D.C. 20301
35 Attn: G. A. Cann

Superintendent
Naval Postgraduate School
Monterey, CA 93940
36 Attn: Library

Commander
Naval Coastal Systems Center
Department of the Navy
Panama City, FL 32407
37 Attn: G. McLeroy

Defense Advanced Research Projects Agency
1400 Wilson Blvd.
Arlington, VA 22209
38 Attn: CDR K. Evans (TTO)

39 Commander
Naval Intelligence Support Center
4301 Suitland Road
Washington, D.C. 20390

Distribution list for ARL-TR-83-41 under Contract N00014-82-C-0049 (cont'd)

Copy No.

40 - 51	Commanding Officer and Director Defense Technical Information Center Cameron Station, Building 5 5010 Duke Street Alexandria, VA 22314
	Woods Hole Oceanographic Institution 86-95 Water Street Woods Hole, MA 02543
52	Attn: R. Spindel
	Science Applications, Inc. 1710 Goodridge Drive McLean, VA 22101
53	Attn: C. Spofford
54	J. Hanna
	Applied Research Laboratory The Pennsylvania State University P. O. Box 30 State College, PA 16801
55	Attn: S. McDaniel
	Marine Physical Laboratory of The Scripps Institution of Oceanography The University of California, San Diego San Diego, CA 92132
56	Attn: F. Fisher
57	G. Shor
	Scripps Institution of Oceanography The University of California, San Diego La Jolla, CA 92037
58	Attn: Library
59	R. Tyce
	Bell Telephone Laboratories, Inc. Whippany Road Whippany, NJ 07961
60	Attn: A. Carter
61	R. Holford
62	D. Romain
	Planning Systems, Inc. 7900 Westpark Drive, Suite 507 McLean, VA 22101
63	Attn: R. Cavanaugh
64	B. Brunson

Distribution list for ARL-TR-83-41 under Contract N00014-82-C-0049 (cont'd)

Copy No.

TRW, Inc.
TRW Defense & Space Systems Group
Washington Operations
7600 Colshire Drive
McLean, VA 22101
65 Attn: R. T. Brown
66 I. Gereben

Defence Scientific Establishment
HMNZ Dockyard
Devonport, Auckland
NEW ZEALAND
67 Attn: K. M. Guthrie

School of Mechanical Engineering
Georgia Institute of Technology
Atlanta, GA 30332
68 Attn: A. D. Pierce

Department of Geology and Geophysics
Geophysical and Polar Research Center
Lewis G. Weeks Hall for Geological Sciences
The University of Wisconsin, Madison
1215 W. Dayton Street
Madison, WI 53706
69 Attn: C. S. Clay

Courant Institute
251 Mercer Street
New York, NY 10012
70 Attn: D. C. Stickler

Bolt, Beranek, & Newman, Inc.
50 Moulton Street
Cambridge, MA 02138
71 Attn: H. Cox

Hawaii Institute of Geophysics
The University of Hawaii
2525 Correa Road
Honolulu, HI 96822
72 Attn: L. N. Frazer

Director
North Atlantic Treaty Organization
SACLANT ASW Research Centre
APO New York 09019
73 Attn: T. Akal

Distribution list for ARL-TR-83-41 under Contract N00014-82-C-0049 (cont'd)

Copy No.

Defence Research Establishment Pacific
FMO Victoria, BC
VOS 1BO CANADA
74 Attn: R. Chapman

Defence Research Establishment Atlantic
9 Grove Street
P. O. Box 1012
Dartmouth, NS
CANADA
75 Attn: D. Chapman

Rosenteil School of Marine and
Atmospheric Science
The University of Miami
10 Rickenbacker Causeway
Miami, FL 33149
76 Attn: H. DeFarrari

Applied Physics Laboratory
The Johns Hopkins University
Johns Hopkins Road
Laurel, MD 20810
77 Attn: J. Lombardo
78 R. Henrick

Department of Ocean Engineering
Massachusetts Institute of Technology
Cambridge, MA 02139
79 Attn: I. Dyer
80 G. Duckworth
81 A. Baggerar

The University of Miami
10 Rickenbacker Causeway
Miami, FL 33149
82 Attn: F. Tappert

Physics Department
The University of Rhode Island
Kingston, RI 02881
83 Attn: C. Kaufman

Department of Electrical Engineering
Polytechnic Institute of New York
Farmingdale, NY 11735
84 Attn: L. B. Felsen

Distribution list for ARL-TR-83-41 under Contract N00014-82-C-0049 (cont'd)

Copy No.

85 I. Tolstoy
Knockvennie, Castle Douglas
S. W. SCOTLAND
GREAT BRITAIN

Department of Geology
The University of Texas at Austin
Austin, TX 78712
86 Attn: C. Wilson

Physics Department
The University of Auckland
Private Bag, Auckland
NEW ZEALAND
87 Attn: A. C. Kibblewhite
88 C. T. Tindle

Chinhae Research Laboratory
P. O. Box 18
Chinhae, Kyeong Nam
KOREA
89 Attn: Jungyul Na

The Lamont-Doherty Geological Observatory
Columbia University
Palisades, NY 10964
90 Attn: R. D. Stoll

Ocean Data Systems, Inc.
Defense Systems
6110 Executive Blvd., Suite 320
Rockville, MD 20852
91 Attn: G. Jacobs
92 P. C. Etter

93 Nancy R. Bedford, ARL:UT

94 Karl C. Foche, ARL:UT

95 Robert F. Gragg, ARL:UT

96 Loyd Hampton, ARL:UT

97 Kenneth E. Hawker, ARL:UT

Distribution list for ARL-TR-83-41 under Contract N00014-82-C-0049 (cont'd)

Copy No.	
98	Stephen G. Houser, ARL:UT
99	Jo B. Lindberg, ARL:UT
100	Robert A. Koch, ARL:UT
101	David Knobles, ARL:UT
102	Stephen K. Mitchell, ARL:UT
103	David W. Oakley, ARL:UT
104	Clark S. Penrod, ARL:UT
105	Richard Pitre, ARL:UT
106	Carol V. Sheppard, ARL:UT
107	Paul J. Vidmar, ARL:UT
108	Library, ARL:UT
109 - 119	Reserve, ARL:UT